nature communications

Article

https://doi.org/10.1038/s41467-026-69804-3

Diverse regulation of functional dimerization of a sugar transporter by different interfacial lipids

Received: 16 December 2024

Accepted: 6 February 2026

Published online: 23 February 2026

Check for updates

Yan Zhang[1,2,7], Weijing Zhao[2,7], Mojie Duan[2] ✉, Yang Shen[3], Jianping Li[4,5], Huayong Xie[2], Qiong Tong[2], Yongxiang Zhao[1,6] & Jun Yang[1,2,6] ✉

Endogenous lipids play essential roles in modulating membrane protein structure and function, yet the molecular mechanisms governing lipid-specific regulation remain elusive. Here, we combine solid-state NMR spectroscopy and molecular dynamics simulations to elucidate how distinct lipids regulate the structure and activity of a membrane protein in a native-like membrane environment. Using *Vs*SemiSWEET as a model system, we determine its high-resolution structure with bound lipids, identifying three lipid types: phosphatidylethanolamine (PE), phosphatidylglycerol (PG), and cardiolipin (CDL). These lipids bind at the monomer-monomer interface, stabilizing the dimeric structure of *Vs*SemiSWEET. Notably, PG and CDL exhibit differential binding modes, with CDL demonstrating a dual interaction mechanism involving both its headgroup and acyl chains that enhances both dimer stability and functional activity. These findings reveal how lipids with different physicochemical properties differentially control membrane protein oligomerization and function, providing a mechanistic framework for lipid-specific regulation.

Specific-binding lipids play a pivotal role in modulating the function, structure, stability, oligomeric state, and conformational dynamics of membrane proteins[1–3], such as ammonia channel (AmtB)[4], osmotic stress-regulated betaine transporter (BetP)[5], multidrug transporter LmrP[6], prokaryotic SthK channel[7], and Na^+/H^+ antiporter NhaA[8]. The high lipid compositional diversity of cellular membranes, combined with the complexity of interactions between bound lipids and membrane proteins, allows for differential regulation of these proteins by multiple bound lipid species[2,9,10]. Distinct structural and chemical properties of lipids, such as variations in acyl chain length and saturation, as well as differences in headgroup chemistry, contribute to the diversity of lipid–protein specific interactions[11,12].

Growing evidence highlights the critical role of specific bound lipid species in modulating the function and structure of membrane proteins. For instance, the KirBac1.1 channel is activated by anionic lipids such as cardiolipin (CDL) and phosphatidylglycerol (PG), but is inactivated by phosphatidylinositol 4,5-bisphosphate (PIP_2)[13]. Additionally, the anionic lipid phosphatidic acid (PA) and the zwitterionic lipid phosphatidylethanolamine (PE) have been reported to selectively bind to the two-pore domain potassium channel K2P4.1, with each lipid featuring non-overlapping interaction sites and distinct regulatory mechanisms[14]. The structural and functional roles of diverse lipid binding were further underscored by recent structural studies of mechanosensitive potassium leak channel TREK1[14], pentameric ligand-

[1]State Key Laboratory of Magnetic Resonance Spectroscopy and Imaging, National Center for Magnetic Resonance in Wuhan, Wuhan Institute of Physics and Mathematics, Innovation Academy for Precision Measurement Science and Technology, Chinese Academy of Sciences, Wuhan, P. R. China. [2]Interdisciplinary Institute of NMR and Molecular Sciences, School of Chemistry and Chemical Engineering, The State Key Laboratory of Refractories and Metallurgy, Wuhan University of Science and Technology, Wuhan, P. R. China. [3]Laboratory of Chemical Physics, National Institute of Diabetes and Digestive and Kidney Diseases, National Institutes of Health, Bethesda, MD, USA. [4]Department of Microbiology, Nanjing Medical University, Nanjing, P. R. China. [5]Laboratory for Pathogen Infection and Control of Jiangsu Province, Nanjing Medical University, Nanjing, P. R. China. [6]University of Chinese Academy of Sciences, Beijing, P. R. China. [7]These authors contributed equally: Yan Zhang, Weijing Zhao. ✉e-mail: mjduan@wipm.ac.cn; yangjun@wipm.ac.cn

gated ion channels (pLGICs)[15,16], and Mycobacterium tuberculosis efflux pump EfpA[17]. These studies reveal the binding of multiple lipid species within the structures of these membrane proteins, demonstrating that the binding of multiple lipids is not merely incidental but often integral to the structural integrity and biological activity of membrane proteins.

Although diverse lipid–protein interactions have been extensively studied across membrane proteins, the role of bound lipids in regulating protein structure and function are still widely debated. Currently, it is challenging to experimentally investigate the specific interactions between lipids and membrane proteins using conventional structural biology methods such as X-ray crystallography, solution NMR spectroscopy, and mass spectrometry. This is primarily because these approaches typically rely on detergent-containing membrane mimetics, which disrupt native lipid–protein interactions in non-native membrane environments. In X-ray crystallography, lipids frequently fail to adopt ordered arrangements due to their high flexibility, rendering them undetectable in membrane protein crystals[6,18]. Similarly, in mass spectrometry, the complexity and overlap of lipid fragmentation spectra impede the clear identification of specific lipids and their interactions[19]. As a result, the specific bound lipid species, their binding sites on proteins, and their functional relevance are often poorly defined for many membrane proteins.

A representative example is the bacterial sugar transporter *Vibrio sp*. SemiSWEET (*Vs*SemiSWEET), a prototypical member of the major facilitator superfamily (MFS)[20]. The SWEET family of transporters is responsible for facilitating sugar uptake across cellular membranes, enabling solute permeation down a concentration gradient. These proteins play essential roles in various biological processes, including nectar secretion, pollen nutrition, and susceptibility to pathogens[21]. Their bacterial homologs, known as SemiSWEETs, are widely distributed among prokaryotes and represent one of the smallest known transporter families. To date, the structures of four distinct SemiSWEETs have been determined by X-ray crystallography in the lipid cubic phase (LCP), revealing three conformational states: outward-open, occluded, and inward-open[22–26]. All four structures exhibit the same dimeric architecture, suggesting that SemiSWEETs consistently function as dimers and employ an alternating-access mechanism for sugar transport.

However, it is important to note that none of these reported crystal structures showed the presence of bound lipids. In contrast, mass spectrometry analysis of *Vs*SemiSWEET in detergent identified tightly bound lipid species, including CDL, PG, and PE. Among these, only CDL was found to regulate *Vs*SemiSWEET dimerization[1,27]. The presence of detergent in these experimental conditions may disrupt the native structure of membrane proteins and interfere with protein–lipid interactions. Additionally, the use of different membrane-mimetic environments, such as detergent micelles versus LCP, may further contribute to the discrepancies in the observed results. Consequently, it is still unclear whether *Vs*SemiSWEET harbors tightly bound lipids in its native membrane environment, where they bind, and what specific functional roles they play. Further experimental investigation is required to elucidate the nature of lipid binding and its functional implications in *Vs*SemiSWEET[28]. In this context, solid-state NMR (ssNMR) has emerged as a powerful technique for determining membrane protein structures and characterizing their lipid interactions at atomic resolution within native-like lipid bilayers[29–32].

In this work, we explore the molecular basis for lipid modulation in *Vs*SemiSWEET through an integrated approach incorporating NMR, additional biochemical experimental techniques, and molecular dynamics (MD) simulations. We identify three co-purifying lipid types: PE, PG, and CDL, among which CDL exhibits the highest binding affinity. Through integrated ssNMR and MD analyses, we determine the structure of lipid-bound *Vs*SemiSWEET in native-like lipid bilayers and resolve the distinct binding sites and interaction modes for each lipid. Our results reveal that PG and CDL exert differential effects on dimer stability and function of *Vs*SemiSWEET via their specific acyl tails and headgroups. These findings provide a mechanistic understanding of how lipids with distinct physicochemical properties differentially regulate membrane protein oligomerization and activity.

Results

Identification of bound lipids co-purified with *Vs*SemiSWEET

SsNMR spectral analysis of *Vs*SemiSWEET liposomes confirmed the presence of bound lipids that co-purified with the protein. The purified protein was successfully reconstituted into total *E. coli* lipid extracts, and resonances for 85 out of 97 residues were assigned using a series of multidimensional ssNMR spectra[33]. To identify these co-purified bound lipids, we performed a ^{13}C-^{13}C combined $R2^{v}_{mathrmn}$-driven (CORD) experiment[34] on uniformly-^{13}C, ^{15}N-labeled *Vs*SemiSWEET. Since the co-purified lipids were ^{13}C-labeled, they generated ^{13}C-^{13}C correlation signals in the CORD spectrum. In contrast, the *E. coli* total lipid extracts used for reconstitution were unlabeled and did not produce such correlations in the spectrum. As shown in Fig. 1a, several cross-peaks were observed in the ^{13}C chemical shift region of 60–75 ppm, corresponding to characteristic chemical shifts of lipid headgroups and glycerol backbone. To rule out the possibility that these signals originated from the protein itself, we employed an unfolding-refolding approach. During this process, ^{13}C-labeled bound lipids were removed during the unfolding procedure, while unlabeled lipids were reintroduced to the protein during the refolding and reconstitution process. Following this treatment, the signals in this region were either absent or significantly weakened, confirming their origin from ^{13}C-labeled bound lipids. Furthermore, Ser and Thr residues are the only amino acids exhibiting intra-residual correlations in this region. The signals of these residues have been unambiguously assigned, confirming that the identified signals arise from co-purified lipids rather than protein-derived signals.

To identify the specific species of the bound lipids, we first measured the ^{13}C chemical shifts corresponding to the headgroups and glycerol backbone of anionic lipid PG, zwitterionic lipids PE, and CDL using ^{1}H-^{13}C HSQC (heteronuclear single quantum coherence) solution NMR spectra of pure lipid standards (Fig. S1 and Table S1)[35]. We then acquired a 2D ^{13}C-^{13}C CORD spectrum of ^{13}C, ^{15}N-labeled *Vs*SemiSWEET with a 500 ms mixing time, optimized to enhance correlation signal intensities from bound lipids (Fig. S2). Although minor chemical shift differences existed between the free and protein-bound states of the lipids, the characteristic α–β correlation patterns allowed us to assign the glycerol backbone and headgroup signals for PE, PG, and CDL[36–38]. Specifically, well-resolved and symmetric correlations at 64.8–42.9, 73.4–69.2, and 72.0–69.0 ppm were unambiguously assigned to the headgroups of co-purified PE, PG and CDL, respectively (Fig. 1b). To further verify these assignments, we prepared a ^{13}C-labeled total *E. coli* lipid extract sample containing no protein. This sample consisted of approximately 57% PE, 15% PG, 10% CDL, and 18% other minor species identified by mass spectroscopy[39]. Notably, this lipid profile is analogous to the native lipid composition of *Vibrio* species[40]. As illustrated in Fig. 1b, the ^{13}C chemical shifts of PE, PG and CDL in the *E. coli* lipid extract align perfectly with those observed for the lipids bound to *Vs*SemiSWEET. This exact signal match provides direct evidence that these three lipid species co-purify with the protein, demonstrating their stable and high-affinity interaction with *Vs*SemiSWEET.

To further identify the bound lipids, we employed 1D ^{31}P solution NMR, a technique that yields distinct chemical shifts for lipid phosphate groups in each lipid type[41–43]. In our spectra, PE, CDL, and PG were identified by their characteristic shifts at −0.20 ppm, 0.22 ppm, and 0.30 ppm, respectively (Fig. S3). As shown in Fig. 1c, the ^{31}P NMR spectra of *Vs*SemiSWEET in detergent micelles verified the co-purification of PE, PG, and CDL. Notably, after a wash with 1% dodecyl-β-D-maltoside (DDM), the ^{31}P signals of PE and PG decreased by 80%

https://doi.org/10.1038/s41467-026-69804-3

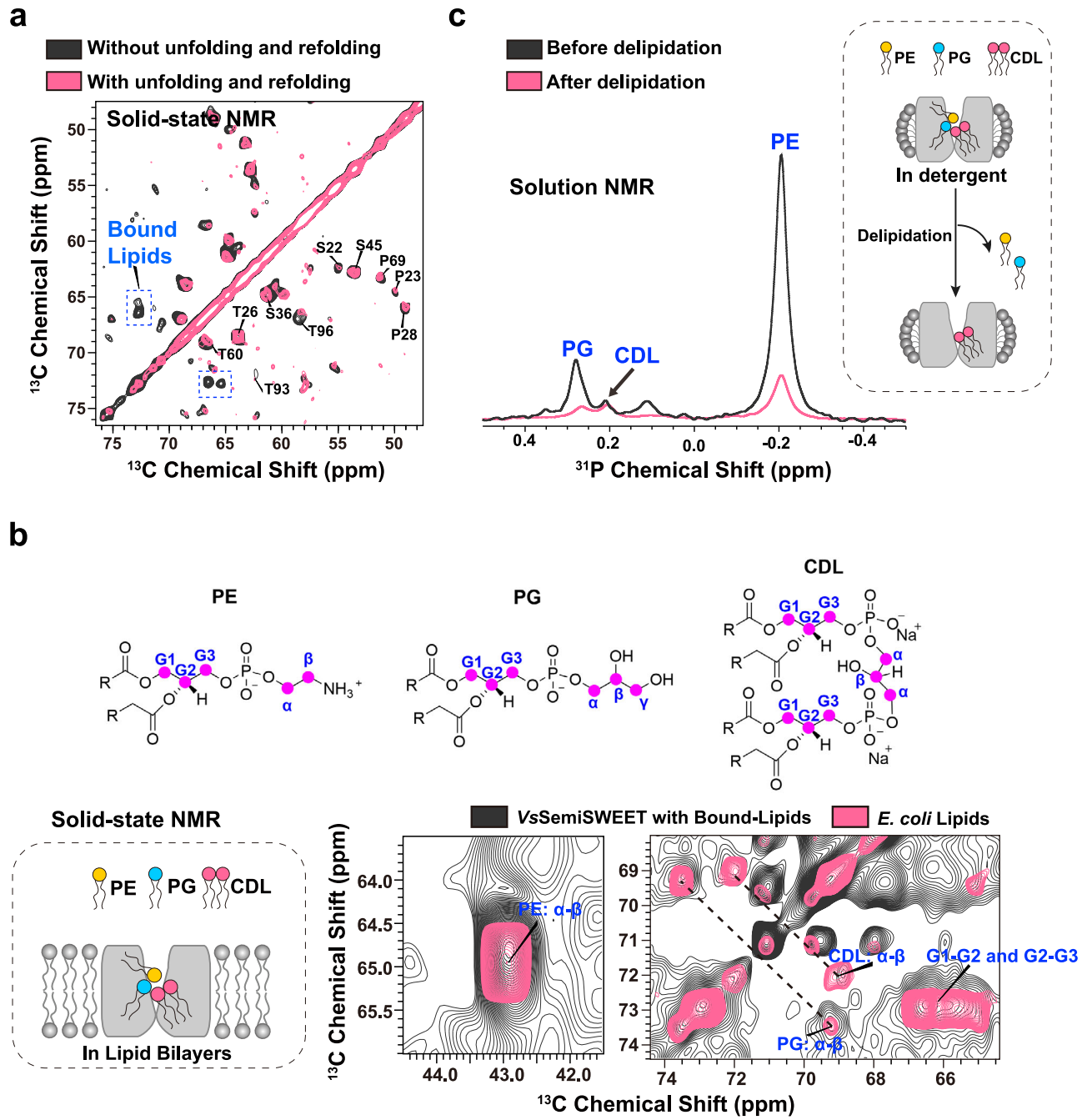

Fig. 1 | Identification of co-purified bound lipids in *Vs*SemiSWEET. a SsNMR 2D CORD ^{13}C-^{13}C spectra (mixing time of 50 ms) of *Vs*SemiSWEET reconstituted into *E. coli* membrane extracts, comparing samples subjected to unfolding-refolding treatment (pink) with native preparations (black). The unfolding-refolding treatment replaces tightly bound ^{13}C-labeled lipids with natural abundance lipids, resulting in the disappearance of lipid-specific signals (blue dotted box). All assigned Ser/Thr backbone resonances are labeled. **b** Molecular structure formulas of PE, PG, and CDL lipids. To validate the bound lipid signals, ssNMR 2D ^{13}C-^{13}C CORD spectrum of ^{13}C-labeled *Vs*SemiSWEET with bound lipids (black) were superimposed to that of pure *E. coli* lipids without the proteins (pink). Homology model illustrating *Vs*SemiSWEET bound with PE, PG, and CDL lipids in lipid bilayers. **c** Solution NMR analysis of lipid binding in *Vs*SemiSWEET. Left: Superimposed 1D ^{31}P NMR spectra of lipids bound to *Vs*SemiSWEET before and after delipidation. Detergent treatment selectively removes loosely bound lipids while preserving tightly bound species. Right: Homology models illustrating *Vs*SemiSWEET in its native lipids-bound state (top) and after delipidation (bottom).

approximately, while the CDL signal showed little reduction, demonstrating that CDL binds more tightly than PE or PG. We extended this analysis to SemiSWEET proteins from *E. coli*, *L. biflexa*, and *Bradyrhizobium* species. Although all three lipids co-purified with these homologs, the binding strength of CDL was consistently lower than that observed for *Vs*SemiSWEET (Fig. S4). This trend agrees with our MD simulations, which also identified CDL binding in these variants but with comparatively weaker interactions (Fig. S5).

Structural characterization of *Vs*SemiSWEET in lipid bilayers using ssNMR

Next, we proceeded to identify the specific lipid-binding sites on *Vs*SemiSWEET. Although the X-ray crystal structure of *Vs*SemiSWEET is available[25], we determined a high-resolution 3D structure of the protein in native-like lipid bilayers to avoid potential artifacts introduced by the non-native detergents used in X-ray crystallography. To obtain the necessary distance restraints for structure determination, we

https://doi.org/10.1038/s41467-026-69804-3

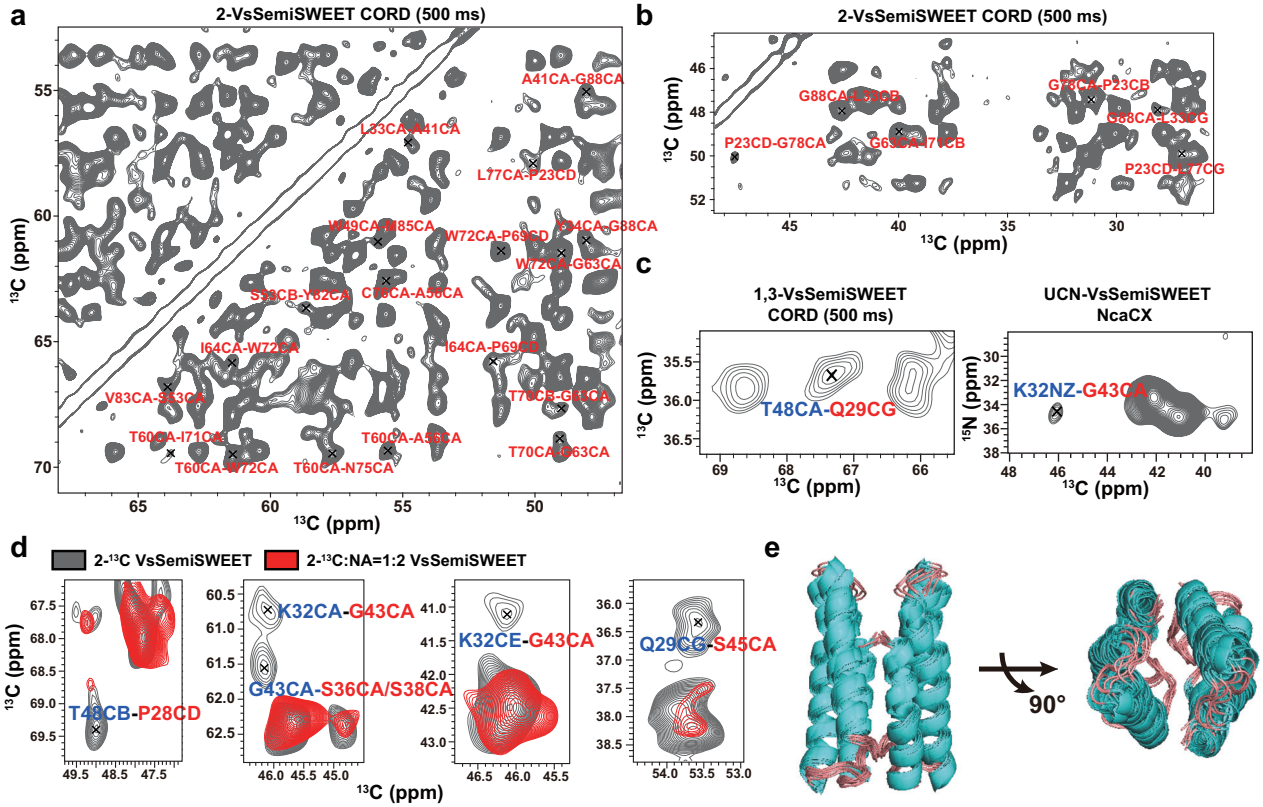

Fig. 2 | Three-dimensional structure of *Vs*SemiSWEET in lipid bilayers determined by ssNMR. a, **b** Selected regions of the 2D ^{13}C-^{13}C CORD spectrum of 2-*Vs*SemiSWEET with a mixing time of 500 ms, illustrating the assignments of the long-range intra-monomer correlations. Cross peaks corresponding to long-range restraints (|i - j|> 5, where i and j represent correlated residues) are labeled in red. **c** Selected regions of the 2D ^{13}C-^{13}C CORD spectrum of 1,3-*Vs*SemiSWEET and the 2D NcaCX spectrum of uniformly-^{13}C, ^{15}N labeled *Vs*SemiSWEET, showing the assignments of the long-range inter-monomer correlations. **d** Superposition of 2D ^{13}C-^{13}C CORD spectra of 2-^{13}C *Vs*SemiSWEET and spin diluted (2-^{13}C:NA = 1:2) *Vs*SemiSWEET samples. Assigned long-range inter-monomer correlations are labeled. **e** Superposition of the ten dimer structures of *Vs*SemiSWEET with the lowest energy in lipid bilayers, with RMSD of 0.9 ± 0.3 Å of the backbone atoms. The N-helix (residues 1–17) structure remains unconverged due to the lack of assigned chemical shifts in residues from 1 to 5 and 12 to 17, which are not shown.

conducted 2D ^{13}C-^{13}C CORD experiments on sparsely ^{13}C-labeled samples. During bacterial protein expression, [2-^{13}C] or [1,3-^{13}C] glycerol was used as the carbon source (denoted as 2-*Vs*SemiSWEET and 1,3-*Vs*SemiSWEET), resulting in significant ^{13}C spin dilution[44]. This dilution greatly improved spectral resolution and suppressed dipolar truncation effect, thereby providing numerous well-resolved cross-peaks corresponding to medium- and long-range distance restraints[45–47]. The "medium-range" and "long-range" correspond to distances between residues where i and j are residue numbers. For medium-range, the distance is defined as $2 \le |i-j| < 5$, while for long-range, it is $|i-j| \ge 5$. Both the 2-*Vs*SemiSWEET and 1,3-*Vs*SemiSWEET samples were prepared using an unfolding-refolding approach to replace the original ^{13}C-labeled co-purified lipids with unlabeled ones, thereby eliminating potential lipid-derived signal interference during restraint assignment. Comparison of the chemical shifts and signal intensities between the refolded and native *Vs*SemiSWEET samples confirmed that the unfolding-refolding process did not perturb the protein structure (Figs. S6 and S7).

As shown in Fig. 2a, b and Fig. S8, the CORD spectra with a 500 ms mixing time exhibit hundreds of well-resolved cross-peaks. However, significant spectral overlap complicates their unambiguous assignment. To address this, we employed a structural template to guide distance restraint determination. We constructed an experimental structural model using CS-Rosetta calculations, inputting chemical shift data and initial distance restraints determined solely based on residue-specific chemical shifts (Table S2). The resulting monomeric structure of *Vs*SemiSWEET exhibits high convergence, with a root mean square deviation (RMSD) of 0.9 ± 0.2 Å for backbone heavy atoms among the ten lowest-energy structures, and is consistent with the AlphaFold3-predicted structure (Fig. S9)[48]. To illustrate how this structural model can resolve assignment ambiguities, we provide an example (Fig. S10). The cross-peak at (70.0, 61.4) ppm in the CORD spectrum of 2-*Vs*SemiSWEET has eight candidate assignments; however, seven possibilities are excluded because their corresponding ^{13}C-^{13}C distances exceed the upper limit (9 Å) for a 500 ms mixing time, leaving only the 4.3 Å correlation between T60 Cα and W72 Cα. Further assignment details regarding the assignment of distance restraints can be found in the Methods Section. In total, we successfully assigned 442 ^{13}C-^{13}C intra-monomer distance restraints, including 117 long- and medium-range restraints (Fig. 2a, b and Fig. S11). Structural calculations performed using Xplor-NIH software with these comprehensive intra-monomer restraints yielded an ensemble of ten structures (selected from 200) with a backbone RMSD of 1.5 Å across all α-helices of the protein (Fig. S10c).

*Vs*SemiSWEET exists as a dimer in lipid bilayers, as demonstrated by our cross-linking experiments (Fig. S12). Assignment of inter-monomer distance restraints, which are critical for determining the dimer structure, is challenging due to potential overlap with intra-monomeric contacts. To address this, we initially assigned inter-monomer distance restraints by excluding intra-monomer contacts based on the monomer structure. All possible intra-monomer distances exceeded the upper limit of 9.0 Å, allowing us to exclude them during distance restraint assignment (Fig. 2c and S13a, b). To further distinguish between intra- and inter-monomer contacts, we prepared a

spin-diluted sample by mixing ^{13}C-labeled monomers with natural abundance (NA) analogs at a 1:2 ratio using an unfolding-refolding approach (Fig. S14a). In this setup, intra-monomer signals are reduced to one-third of their original intensity in uniformly labeled samples, while inter-monomer signals were absent (Fig. S14b). By comparing the signal intensities in 2D ^{13}C-^{13}C spectra of 2-*Vs*SemiSWEET and the spin-diluted [(1:2)2-^{13}C/NA] *Vs*SemiSWEET samples, we unequivocally identified cross-peaks originating from inter-molecular contacts (Fig. 2d).

The analysis of CORD spectra from a diluted sample revealed six ambiguous inter-monomer distance constraints. These constraints were used to construct an initial dimer structural model using the docking module of Xplor-NIH. Further details on the homodimer construction are provided in the Methods Section. Utilizing this initial model, thirteen unambiguous and eight additional ambiguous inter-monomer contacts were identified. The strategy for resolving intra- versus inter-monomer contact ambiguity is illustrated in Figs. S13c and S15, with examples of assignments for Q29CG-T48CA and K32CA-G43CA restraints. All inter-monomer long-range distance restraints are listed in Table S3. A total of 21 inter-monomer and 442 intra-monomer distance restraints, along with 78 backbone torsion angles predicted by the TALOS+ program using assigned chemical shifts (Table S4), were employed to calculate 1024 dimer structures of *Vs*SemiSWEET using Xplor-NIH. For further details on the structure calculations, refer to the experimental section. Among the calculated structures, the ten lowest-energy structures exhibited high convergence, with a backbone RMSD of 0.9 ± 0.3 Å (Fig. 2e).

Hydrogen/deuterium (H/D) exchange experiments revealed a solvent-accessible cavity between the two monomers near the periplasmic region, supporting an outward-open conformation (Fig. S16). The overall ssNMR structure is similar to the crystal structure (Fig. S17), with a backbone RMSD of 2.0 Å across well-ordered regions (residues 17–39, 46–67, and 70–92). Notably, a key structural feature in the ssNMR structure is the pronounced kink at Pro29 within the conserved PQ-loop motif of TM1, which divides the helix into TM1a and TM1b segments. Importantly, while bound lipids remained physically present in the *Vs*SemiSWEET structural determination samples, their structural constraints were removed by substituting ^{13}C-labeled lipids with natural abundance lipids during the unfolding-refolding process. Consequently, the bound lipids are absent in the determined structures, leaving empty coordinates due to the lack of distance restraints.

Characterization of lipid interactions with *Vs*SemiSWEET in native-like lipid bilayers

To investigate the interactions between *Vs*SemiSWEET and its bound lipids, we performed 2D CORD spectra of uniformly ^{13}C, ^{15}N-labeled *Vs*SemiSWEET using a long mixing time of 500 ms. The chemical shift at 72.8 ppm was uniquely assigned to the G2 nuclei of the central glycerol moiety in lipids. Therefore, any cross-peaks at this chemical shift in the 2D ^{13}C-^{13}C spectrum of lipid-bound *Vs*SemiSWEET must represent either lipid–lipid or lipid–protein correlations. A ^{13}C-^{13}C spectrum of uniformly ^{13}C-labeled *E.coli* lipid extracts, which contains no protein signals, serves as a reference to distinguish between lipid–lipid and lipid–protein interactions. As shown in Fig. 3a, additional peaks observed at 72.8 ppm in the *Vs*SemiSWEET spectra correspond specifically to lipid–protein correlations. Based on the correlated chemical shifts of these peaks (Fig. S18), we identified residues S22, Q29, K32, H37, E39, H40, C76, and A84 as potential interaction sites for lipid G2 nuclei, as both the main-chain and side-chain ^{13}C atoms of these residues exhibit correlation with the G2 nuclei of lipids. Critically, the observation of these lipid–protein cross-peaks in the dipolar-coupling-based experiments imply lipid binding times in the microsecond range or longer but exclude shorter lifetimes, which is the timescale of the relevant dipolar couplings that drive spin diffusion[37].

To assign these lipid–protein correlated peaks, we carried out MD simulations to identify potential lipid-binding sites on *Vs*SemiSWEET. We conducted 5-μs all-atom MD simulations using the ssNMR structure of *Vs*SemiSWEET in lipid bilayers as the starting structure. The average residence time of different lipids at each residue of the SemiSWEETs was calculated to evaluate their binding ability (Fig. 3b and Fig. S19). The results indicated that CDLs exhibited stronger binding ability to *Vs*SemiSWEET compared to PEs, which is consistent with our experimental observations (Fig. 1c). Analysis of the MD simulations highlighted that residues interacting with CDL were predominantly located at the monomer–monomer interface and near transmembrane regions. Notably, basic residues K32, H37, and H40 in the intracellular region demonstrated significantly stronger interactions with CDL compared to other residues (Fig. 3b).

To validate these findings, we mutated the three basic residues K32, H37, and H40 to basic-to-neutral substitutions (K32A, H37A/H40A, and K32A/H37A/H40A). We then assessed the effects of these mutations on lipid binding using 1D ^{31}P solution NMR spectra of the mutated *Vs*SemiSWEET solubilized in micelles. As shown in Fig. 3c, the signal intensities for PE, PG, and CDL lipids all decreased in these mutants, indicating that these lipids bind at the interface between the two monomers. However, while signals from PE and PG persisted, nearly no signals were observed for CDL in the K32A/H37A/H40A mutant. This suggests that CDL exclusively binds at the monomer–monomer interface, whereas PE and PG bind both at the interface and the vicinity of transmembrane regions. These findings align with a recent MD simulation study on *Vs*SemiSWEET, which demonstrated that CDL molecules bind in sufficient numbers to the dimer interface on the cytoplasmic side[28].

To further elucidate the nature of the interaction between bound lipids and these basic residues, we constructed a K32R mutant, which involved a basic-to-basic substitution (Fig. 3d). As expected, the lipid signals observed in the 1D ^{31}P spectrum of the K32R mutant were nearly identical to those of the wild-type *Vs*SemiSWEET, indicating that this basic-to-basic mutation does not significantly disrupt the interaction between the residues and lipids. This finding supports the conclusion that their interactions are predominantly mediated by electrostatic forces. Moreover, in contrast to the dipolar-coupling-based signals from glycerol backbones and headgroups of the bound lipids, which indicate that these groups exhibit structural rigidity on a micro- to millisecond timescale, the signals observed in scalar-coupling-based ssNMR spectra suggest a high degree of flexibility on submicrosecond timescales[49]. As shown in Fig. S20, the tail carbons of lipids in *Vs*SemiSWEET were detected in a 2D ^{1}H-^{13}C INEPT spectrum, indicating the flexibility of the lipid acyl chains. Finally, to generate a composite structural model that incorporates the missing lipid coordinates, we performed molecular docking. This placed two CDL molecules at the dimer interface (Fig. 3e). The docking model revealed that the lipid headgroups establish contacts with basic residues K32, H37, and H40, forming several hydrogen bonds. These findings underscore that lipid binding is predominantly mediated through electrostatic interactions between lipid headgroups and basic residues within the dimer interface.

Bound lipids influence the dimer stability of *Vs*SemiSWEET in lipid bilayers

Dimerization is crucial for enabling *Vs*SemiSWEET to efficiently transport sugars across cellular membranes[21]. To examine how lipid binding influences dimer stability, we conducted ssNMR, biochemical experiments, and MD simulations. As shown in Fig. S20, *Vs*SemiSWEET maintains its dimeric state in the *E. coli* cellular membrane, in proteoliposomes, and when affinity-purified in detergent micelles (0.3% DM), as demonstrated by SDS-PAGE analysis (SDS-resistant). However, mutating the key interfacial basic residues K32, H37, and H40 to

https://doi.org/10.1038/s41467-026-69804-3

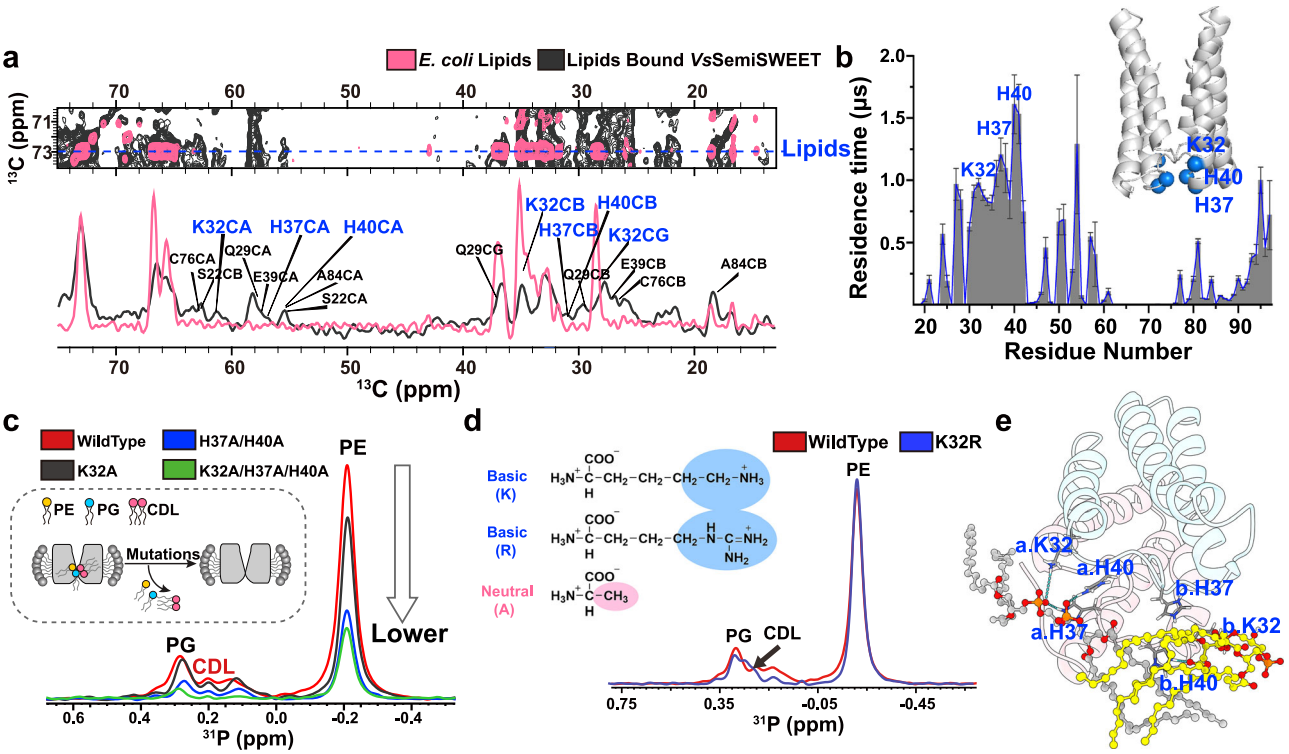

Fig. 3 | Analysis of interactions between bound lipids and *Vs*SemiSWEET. **a** Potential lipid-binding sites identified by ssNMR. Overlay of 2D ^{13}C-^{13}C CORD spectra for *Vs*SemiSWEET bound with lipids (black) and pure ^{13}C-labeled *E. coli* lipid extracts (pink). The *Vs*SemiSWEET spectrum exhibits additional peaks at 72.8 ppm (assigned to lipid G2), indicating lipid–protein interactions. Possible assignments of these additional peaks are labeled based on the residue-specific backbone and side-chain chemical shifts. **b** MD simulation-derived lipid-binding sites. Residence time histograms of CDL at distinct binding sites. The ssNMR structure of *Vs*SemiSWEET in lipid bilayers is shown as a cartoon, with lipid-binding sites rendered as space-filling models. The error was calculated as the standard deviation from three replicate simulations. Source data are provided as a Source Data file. **c** Validation of lipid-binding sites by solution NMR. Superimposed 1D ^{31}P spectra of wild-type *Vs*SemiSWEET and mutants (K32A, H37A/H40A, and K32A/H37A/H40A). The arrow denotes reduced ^{31}P signal intensity in mutants, implicating key residues in lipid binding. **d** Solution NMR analysis of protein–lipid interaction type. Superimposed 1D ^{31}P spectra of wild-type *Vs*SemiSWEET and K32R mutant. **e** Molecular docking of CDL with *Vs*SemiSWEET, illustrating interaction interfaces.

alanine (single or combined mutants) caused a predominant monomeric migration on SDS-PAGE gels (Fig. 4a), whereas the charge-preserving K32R mutant retained its dimeric form. Furthermore, size-exclusion chromatography of these mutants exhibited a monodisperse peak similar to that of wild-type *Vs*SemiSWEET (Fig. 4b), indicating that these alanine mutants still elute as dimers in solution. The SDS-induced dissociation during SDS-PAGE analysis reflects a lipid-dependent stabilization of the dimer interface. Consistent with this finding, thermal stability assays revealed that lipid binding enhances the structural stability of *Vs*SemiSWEET (Fig. S22). We also acquired ssNMR spectra of the H37A/H40A and K32A/H37A/H40A mutants to examine the conformations of the protein in the absence of lipid binding. As shown in Fig. 4c, d, the signals in the 2D ^{15}N-$^{13}C\alpha$ NCA spectrum of these mutants exhibited broader linewidths than those of the wild-type, indicating conformational heterogeneity without lipids binding. Moreover, the disappearance of signals from the mutated sites and their neighboring residues, along with the loss of signals from many other residues, suggests increased conformational dynamics and flexibility in the absence of bound lipids. To further evaluate the structural consequences of disrupting lipid interactions, we carried out enhanced sampling simulations to investigate the stability of the H37A/H40A mutant. The resulting free energy landscape (Fig. S23) shows that the mutant dimer is substantially destabilized: it no longer adopts the lowest-energy conformation characteristic of the wild-type protein, and no stable inter-residue interactions persist at the dimer interface. Collectively, these results highlight the importance of lipid binding in sustaining the stability and structural integrity of the *Vs*SemiSWEET dimer, likely through specific interactions at the monomer–monomer interface.

We further employed MD simulations with enhanced sampling to delineate the mechanism by which lipids modulate dimerization. We characterized the free energy landscapes of CDL-bound and lipid-free *Vs*SemiSWEET (Fig. S24). Representative conformations of the lowest free energy state for both systems are shown in Fig. 4e, f, respectively. Compared to the ssNMR structure, the representative lowest-energy conformation of the lipid-free dimer showed fewer interfacial contacts and only rare, weak interprotomer interactions (Fig. S25). In contrast, the CDL-bound dimer adopted a conformation closely matching the ssNMR structure, with stable interactions across the binding interface (Fig. 4g). These results demonstrate that CDL binding enables the stabilization of a robust dimeric interface for *Vs*SemiSWEET.

Differential regulations of interfacial CDL and PG on the structure and function of *Vs*SemiSWEET

Since three distinct lipid types (CDL, PE, and PG) bind to the dimer interface of *Vs*SemiSWEET, we used an unfolding-refolding approach to selectively deplete tightly bound CDL, allowing us to isolate the structural and functional effects of different lipid compositions. As shown in Fig. S26, fully denatured *Vs*SemiSWEET can refold into dimers in the presence of either PE/PG or PE/PG/CDL mixtures. This observation indicates that both PE/PG and PE/PG/CDL lipid combinations support dimer formation, suggesting functional similarity between these lipid types in stabilizing the protein structure. However, MD simulations revealed fundamentally different binding modes for PG

https://doi.org/10.1038/s41467-026-69804-3

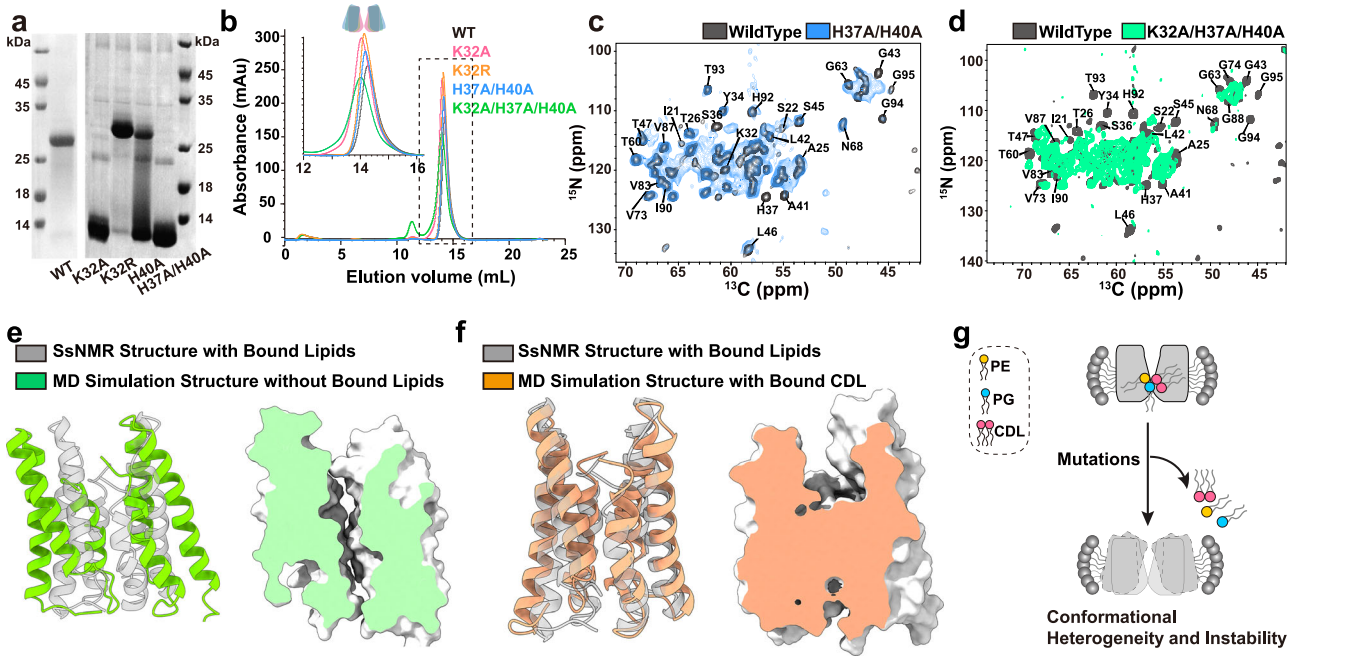

Fig. 4 | Lipid binding modulates the oligomeric state and conformation of *Vs*SemiSWEET. a Oligomeric stability analysis: SDS-PAGE results for wild-type *Vs*SemiSWEET, the K32R and lipid-binding-deficient mutants (K32A, H40A, and H37A/H40A) mutants, reconstituted in proteoliposomes. The gels shown are representative of three independent experiments. Source data are provided as a Source Data file. **b** Oligomeric state analysis: Size-exclusion chromatography profiles comparing wild-type *Vs*SemiSWEET with its variants. Source data are provided as a Source Data file. **c**, **d** Conformational analysis: Superposition of 2D ^{15}N-^{13}Cα spectra of wild-type *Vs*SemiSWEET and the H37A/H40A and K32A/H37A/H40A mutants. **e** MD simulation (lipid-free state) versus ssNMR structure: representative MD conformation of the dimeric *Vs*SemiSWEET without bound lipids, overlaid with the ssNMR-derived structure (lipid-bound). **f** MD simulation (CDL-bound state) versus ssNMR structure: representative MD conformation of the dimeric *Vs*SemiSWEET with bound CDL, overlaid with the ssNMR-derived structure (lipid-bound). **g** Schematic representation of the effect of lipid-binding-site mutations on the oligomeric stability and conformational state of *Vs*SemiSWEET.

and CDL (Fig. 5a). Compared to PG, CDL forms more stable interactions with the protein, particularly through hydrogen bonding (Fig. S27). For example, the hydrogen bond occupancy between CDL and the H40 residue reaches 64%, whereas the maximum hydrogen bond occupancy between PG and H40 is only 23%. This disparity stems from CDL's structure: its headgroup bears two negatively charged phosphate groups, creating a strong electrostatic surface that interacts tightly with adjacent basic residues (K32, H37, and H40) on the protein. This specific interaction underlies CDL's high-affinity binding and its critical role in structural stabilization.

Importantly, MD simulations revealed that the tail chains of PG preferentially penetrate the cavity between the two monomers while their headgroups remain spatially confined at the dimer interface of *Vs*SemiSWEET (Fig. 5a, c). By engaging specific residues within this cavity, the PG tails effectively disrupt inter-monomer packing. In contrast, CDL exhibits a distinct binding mode; its bulky hydrophobic tail cannot accommodate the cavity due to steric constraints (Fig. S28). Instead, CDL tails localize to the outward surface of *Vs*SemiSWEET, promoting a tightly packed dimeric interface. The interaction strength between *Vs*SemiSWEET residues and CDL or PG lipids at the interface was quantitatively evaluated based on contact probability differences. As shown in Fig. 5b, PG lipids predominantly interact with residues located on transmembrane helix 1 (TM1), the N-terminal region of TM2, and the C-terminal region of TM3. Notably, key residues (S22, T26, Q29, L33, S36, T48, Y52, and Y82) exhibited higher lipid contact probabilities in the PG-bound state. These residues are predominantly positioned along the inner faces of the transmembrane helices, further supporting the deep penetration of PG lipid tails into the *Vs*SemiSWEET inner cavity. Additionally, we computed the in-plane density of lipid tail carbon atoms in the membrane. As illustrated in Fig. S29, lipid molecules in the PG-bound *Vs*SemiSWEET system penetrate into the dimer interior and occlude the central pore of the protein.

To experimentally validate the distinct binding modes of PG and CDL, we prepared two ssNMR samples: sample I (with a combination of PE, PG, and CDL lipid binding) and sample II (with a combination of PE and PG lipid binding). The preparation procedures for both samples are shown in Fig. S30. Several critical aspects should be noted: First, the lipid bilayers of both samples are composed of PE and PG lipids to exclude the influence of other environmental lipids on the structure of *Vs*SemiSWEET. Second, binding affinities of different lipids to *Vs*SemiSWEET, calculated by MM/GBSA[50], indicated that the binding ability of CDL to *Vs*SemiSWEET is ~215 times that of PG and about 3600 times that of PE (Fig. S31). These predicted results align with observations from the above delipidation experiments (Fig. 3e). Third, during the refolding, excess PE/PG or PE/PG/CDL was added to fully refold and reassemble the denatured *Vs*SemiSWEET into a dimeric form, favoring binding of lipids with higher affinities. Together, our results indicate that CDL primarily modulates the structure of *Vs*SemiSWEET in Sample I, while PG exhibits a more pronounced regulatory effect in Sample II.

To probe the distinct structural effects of CDL versus PG binding, we acquired ssNMR spectra for Sample I (PE/PG/CDL) and Sample II (PE/PG only). Chemical shift perturbations (CSPs) greater than 0.3 ppm were considered significant, given the high spectral resolution and reproducibility of the ssNMR spectra (Fig. S6). Figure S32 presents the superimposition of the 2D ^{15}N-^{13}Cα and ^{13}C-^{13}C spectra of *Vs*SemiSWEET in samples I and II. While most peaks showed negligible CSPs, some peaks exhibited significant CSPs (Fig. 5d). As shown in Fig. 5e, multiple transmembrane residues of *Vs*SemiSWEET exhibited significant CSPs in sample II compared to sample I, including S22, T26, Q29, L33, S36, T48, Y52, Y82, V86, and I89. These CSP patterns show strong

https://doi.org/10.1038/s41467-026-69804-3

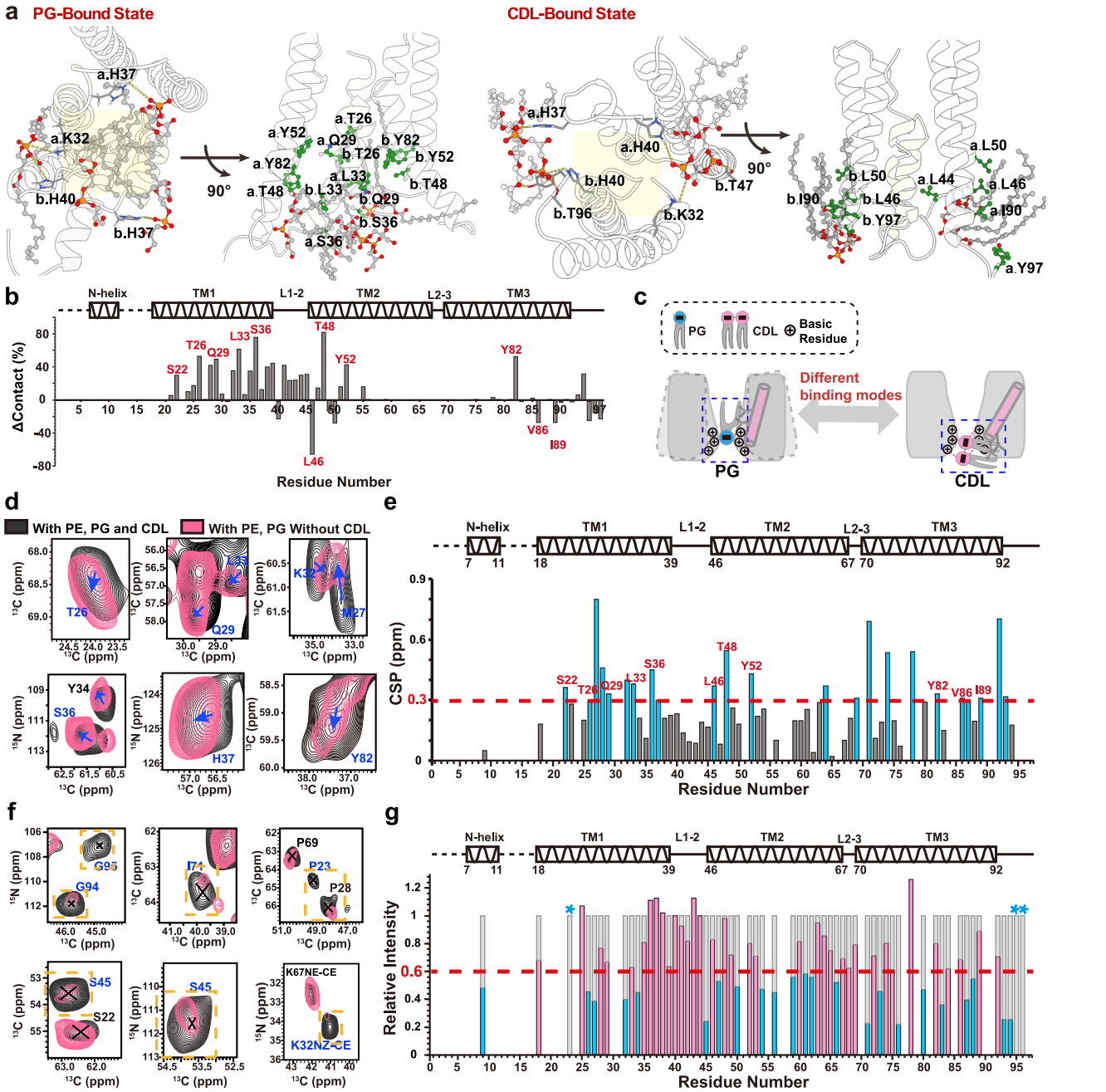

Fig. 5 | Regulatory role of PG and CDL binding in *Vs*SemiSWEET, revealed by MD simulations (a, b) and ssNMR experiments (d–g). a Distinct lipid-binding modes of PG and CDL to *Vs*SemiSWEET analyzed by MD simulations. Left: Residues interacting with lipid headgroups (PG/CDL phosphate groups: orange phosphorus, red oxygen). Right: Residues contacting lipid tails (highlighted in green). Regions with cavity-localized interactions are marked by yellow shading. **b** Contact probability differences of residues with lipids between PG-bound and CDL-bound *Vs*SemiSWEET studied by MD simulations. Source data are provided as a Source Data file. **c** Schematic comparison of PG and CDL binding mechanisms. The acyl tails of PG penetrate the central interfacial cavity, disrupting dimer stability. In contrast, the acyl tails of CDL align along the outer dimer surface, reinforcing the dimeric interface. **d** SsNMR validation of lipid-binding modes. Superimposition of 2D ^{15}N-^{13}Cα and ^{13}C-^{13}C spectra of *Vs*SemiSWEET in samples I (CDL-dominant modulation) and II (PG-dominant modulation). Assigned isolated resonances are labeled, and representative pronounced shifts in chemical shifts are indicated by blue arrows. **e** Quantitative analysis of the CSPs of residues induced by different lipid binding. Plot of the ^{15}N and ^{13}C CSPs between *Vs*SemiSWEET in samples I and II as a function of residue number. Horizontal lines at 0.3 ppm indicate the threshold for significant CSPs. Residues exhibiting both significant CSPs and MD-predicted lipid contact probability differences (PG- versus CDL-bound states) are marked in red. **f** Superimposition of 2D ^{15}N-^{13}Cα and ^{13}C-^{13}C spectra of *Vs*SemiSWEET in samples I and II, with peaks that show significantly reduced signal intensity marked with orange dotted boxes. Source data are provided as a Source Data file. **g** Quantitative analysis of changes in signal intensity of residues induced by different lipid binding. Relative intensities of signals resolved in ^{15}N-^{13}Cα and ^{13}C-^{13}C spectra of *Vs*SemiSWEET in sample II (pink and blue bars), normalized by the corresponding signal intensities in sample I (gray bars). Dotted lines represent relative signal intensities of 0.6. Residues with relative intensities lower than 60% are colored blue, and signals that became unobservable in sample II are marked with blue asterisks. The secondary structures of *Vs*SemiSWEET in lipid bilayers are illustrated at the top of the figure. Source data are provided as a Source Data file.

https://doi.org/10.1038/s41467-026-69804-3

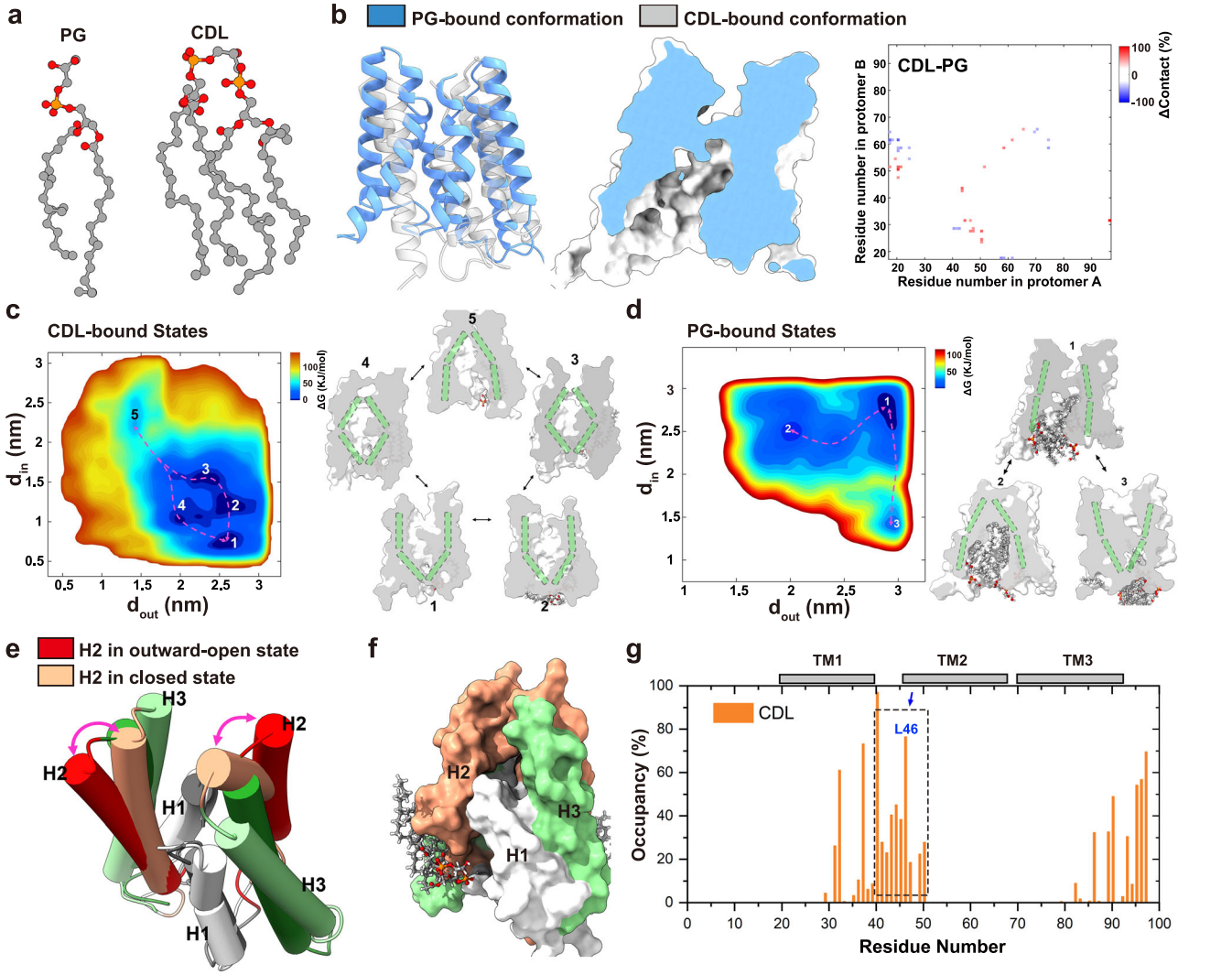

Fig. 6 | Functional regulation of *Vs*SemiSWEET by different lipid binding. **a** Molecular structures of the lipids POPG and CDL. **b** Representative conformations of PG-bound dimeric *Vs*SemiSWEET, illustrating intermolecular residue contacts compared to CDL-bound *Vs*SemiSWEET. **c** Free energy landscape (FEL) of CDL-bound *Vs*SemiSWEET as a function of the open sizes of the outward gate (d_{out}) and inward gate (d_{in}). Here, d_{out} corresponds to the distances between the Cα atoms of residues Y62 on the two protomers, while d_{in} corresponds to the center-of-mass (COM) distances between the Cα atoms of residues L42–L44 on the two protomers. Representative structures of the states observed on the FEL are shown. **d** FEL of PG-bound *Vs*SemiSWEET as a function of the opening size of outward gate and inward gate. **e** Representative conformations of the outward-open and inward-open states. The helices of the outward-open structure are colored dark gray (TM1), red (TM2), and dark green (TM3). The helices of the inward-open structure are colored light gray (TM1), light orange (TM2), and light green (TM3). **f** illustration showing that the tails of CDL primarily interact with TM2 of *Vs*SemiSWEET. **g** Contact probability of bound CDL lipids with the residues of *Vs*SemiSWEET. The black dashed box indicates the region with a high density of contact residues. Source data are provided as a Source Data file.

correlation with our MD simulation results, where the same residues demonstrated the highest differences in lipid contact probability between the PG-bound and CDL-bound states (Fig. 5b). This consistency between experimental CSP data and MD simulation predictions suggests these residues participate in distinct lipid–protein interactions depending on the bound lipid species. The structural differences between CDL and PG likely contribute to their distinct interaction patterns. The larger size of CDL prevents its hydrophobic tails from drilling into the cavity of *Vs*SemiSWEET. In contrast, PG has a smaller steric hindrance, allowing its tails to penetrate deeply into the protein's cavity. This deeper penetration facilitates direct interactions between PG and inner cavity residues, resulting in significant CSPs in these transmembrane residues. Additionally, Fig. 5f and the bar diagram in Fig. 5g showed that the signal intensities of many residues decreased and, in some cases, became unobservable in the dipolar-coupling-based spectra of sample II. This reduction can be attributed to the enhanced mobility and reduced structural stability of these residues in the absence of CDL binding.

To link the influence of dimer formation of different lipid binding to the functional implications, we analyzed the detailed intermolecular interactions and free energy landscapes of *Vs*SemiSWEET binding with various lipids (Fig. 6a). All-atom MD simulations revealed that while PG binding, unlike CDL, does not hinder *Vs*SemiSWEET monomer dimerization but results in more disordered residue arrangements at the dimeric interface and weaker inter-monomeric interactions compared to CDL-bound *Vs*SemiSWEET (Fig. 6b). Moreover, the RMSD distribution further confirms that the CDL-bound system stabilizes a dimer conformation closely matching the ssNMR-resolved structure of *Vs*SemiSWEET, whereas the PG-bound dimer is more heterogeneous (Fig. S33). These findings align with ssNMR data (Fig. 5f, g), which indicate greater dynamics and heterogeneity in the PG-bound dimer. Furthermore, both MD simulation and experimental findings

demonstrate that PE exerts a regulatory effect similar to PG, promoting dimerization but also inducing conformational heterogeneity and instability in the resulting dimers (Fig. S34).

The regulatory effects of different types of lipids on the function of *Vs*SemiSWEET was characterized by MD simulations. As proposed by Feng et al., sugar transport by SemiSWEETs follows a "free ride" mechanism[23]. This mechanism involves spontaneous transitions between outward-open, occluded, and inward-open configurations, facilitating sugar passage from extracellular to intracellular environments. Our analysis of the free energy landscape identified key functional states in CDL-bound *Vs*SemiSWEET: outward-open (states 1 and 2), occluded (states 3 and 4), and inward-open (state 5) structures (Fig. 6c). The outward-open states correspond to the lowest free-energy minima and are thus the most populated, whereas the inward-open state lies at a significantly higher energy and is scarcely populated. This is consistent with our ssNMR findings, where inward-open structures were undetected. These results indicate that CDL binding enables *Vs*SemiSWEET to transition between essential functional states, enhancing its activity via the "free ride" mechanism. In stark contrast, the free energy landscape of PG-bound VsSemiSWEET shows no such conformational transitions (Fig. 6d). The lowest free energy minimum for PG-bound *Vs*SemiSWEET corresponds to a nonfunctional state with an intramembrane cavity filled by PG tails. This suggests that PG creates steric hindrances that not only obstruct ligand passage but also impede the transition cycle between functional states.

The gating mechanism of *Vs*SemiSWEET differs significantly from those observed in its homolog, *L. biflexa* SemiSWEET (*Lb*SemiSWEET)[23,25]. In *Lb*SemiSWEET, Feng et al. proposed that TM1 undergoes kinking at the central proline residue, disrupting interactions with TM3 and facilitating conformational transitions between outward-open, occluded, and inward-open states. In *Vs*SemiSWEET, however, TM2 serves as the primary driver of structural transitions between closed and open states at both extracellular and intracellular gates (Fig. 6e). The rocking motion of TM2 in opposite directions across the two protomers of the *Vs*SemiSWEET dimer controls the opening of both the outward and inward gates (Fig. S35). This motion is closely linked to lipid interactions, as shown by our analysis of residue–lipid interactions in all-atom MD simulations. The results reveal extensive interactions between TM2 and CDL (Fig. 6f, g), where the hydrophobic tails of CDL interact with the outer surface of TM2, modulating helical orientational fluctuations. Experimental evidence supports this mechanism: residue L46 in the TM2 region, which exhibits the highest probability of contact with CDL, shows significant CSPs in sample II (lacking CDL) compared to sample I (Fig. 5g). Together, these findings underscore a critical and specific role for CDL in enabling the functional transition cycle of *Vs*SemiSWEET.

Discussion

In this study, we have identified the bound lipids PE, PG, and CDL in *Vs*SemiSWEET by characteristic ^{13}C chemical shifts from the glycerol backbone and headgroup in ssNMR spectra, as well as ^{31}P chemical shifts of phosphate groups in solution NMR spectra. These identifications were further validated through delipidation experiments. The binding of PE, PG and CDL to *Vs*SemiSWEET aligns with the findings from previous studies that used native mass spectrometry[1,27]. In contrast, no bound lipids were identified in the crystal structure of *Vs*SemiSWEET[25], likely due to the high mobility of these lipids. Moreover, the choice of detergent used for solubilization can significantly affect lipid binding. Recent studies suggest that different detergent species can impede the cooperative binding of lipids to membrane proteins[17,51–53]. It remains unclear whether the samples in DDM or LCP detergent for the crystal characterization of *Vs*SemiSWEET contain co-purified lipids. While we have demonstrated the binding modes of individual lipids, such as PG and CDL, to *Vs*SemiSWEET, the actual binding interactions are likely more complex. Based on both ssNMR and solution NMR experimental results, it is plausible that the binding involves a combination of two or more different types of lipids at the interface of the monomers. This complexity warrants further investigation to fully understand the lipid interactions with *Vs*SemiSWEET.

Lipid–protein specific interactions play a critical role in regulating the sugar transport activity of SemiSWEETs, which function as transporters by assembling into dimers and cycling through outward-open, occluded, and inward-open conformations[54]. CDL, a phospholipid characterized by its dimeric structure with four acyl chains and two phosphate groups, has been shown to play a pivotal role in modulating the oligomerization and conformational dynamics of *Vs*SemiSWEET. The headgroups of CDL molecules bind at the monomer–monomer interface, coordinating the dimerization process of *Vs*SemiSWEET protomers to enable the formation of dimers with a proper and stable conformation that facilitates sugar transport. Furthermore, the four acyl chains of the CDL influence its function in two distinct ways: first, their large size prevents them from entering the transmembrane cavity, thereby avoiding interference with intermolecular interactions; second, the hydrophobic nature of these chains facilitates interaction with transmembrane helix 2, enhancing the transport turnover of *Vs*SemiSWEET. Importantly, various studies have indicated that the interaction between proteins and CDL may depend on the specific way on properties of CDL acyl chains[55]. For example, α-synuclein binding to CDL is significantly influenced by the nature of CDL's acyl side chains: complete saturation drastically reduces affinity, whereas the removal of a double bond increases it[56]. These findings underscore that CDL acts as a regulatory factor in membrane proteins not only through the stabilizing interactions provided by its headgroups but also due to the structural characteristics of its four acyl chains. Collectively, this highlights the critical importance of CDL–protein interactions in modulating SemiSWEET-mediated sugar transport activity.

Dimerization is a prerequisite for *Vs*SemiSWEET to achieve transmembrane sugar transport, as it forms the functional unit required for substrate translocation[23]. The two protomers create a central pathway that enables selective sugar movement across the membrane, with the transport mechanism relying on coordinated conformational changes between monomers, generating an alternating-access mechanism. Disruption of dimerization impairs this conformational switching, leading to a loss of transport activity, underscoring the essential role of dimerization in the function of SemiSWEETs. Notably, the dimer interface is stabilized by interactions with lipids such as CDL, which is critical for maintaining the dimer conformation of *Vs*SemiSWEET. Extensive studies have demonstrated that lipid binding plays a universal regulatory role in membrane protein oligomerization, which is crucial for structural stability and functional integrity[1,12,57]. In this study, we found that, similar to CDL, PE and PG lipids promote dimer formation of *Vs*SemiSWEET. Further insights from ssNMR and MD simulations reveal that CDL tails localize to the outer surface of *Vs*SemiSWEET, enhancing inter-monomer interactions and stabilizing the dimeric structure while facilitating its functional transition cycle; in contrast, PG tails penetrate deep into the protein cavity, disrupting interprotomer interactions and impeding functional conformational switching. This observation aligns with previous findings on the Na^+/H^+ antiporter, where CDL was identified as the optimal lipid for promoting dimer assembly, stability, and functional integrity compared to other types of lipids[58].

The different binding modes observed for PG and CDL lipids can be attributed to their molecular architectures. Cellular membranes exhibit a highly diverse lipid composition, which has the potential to modulate the structure and function of membrane proteins through various lipid–protein interactions[59]. It is interesting to compare the binding modes of PG and CDL to the protein, as well as their respective influence on the structure and function of the protein. One molecule of CDL is roughly equivalent to two PG molecules, but it features a connection between the glycerol backbone of the two PG headgroups.

https://doi.org/10.1038/s41467-026-69804-3

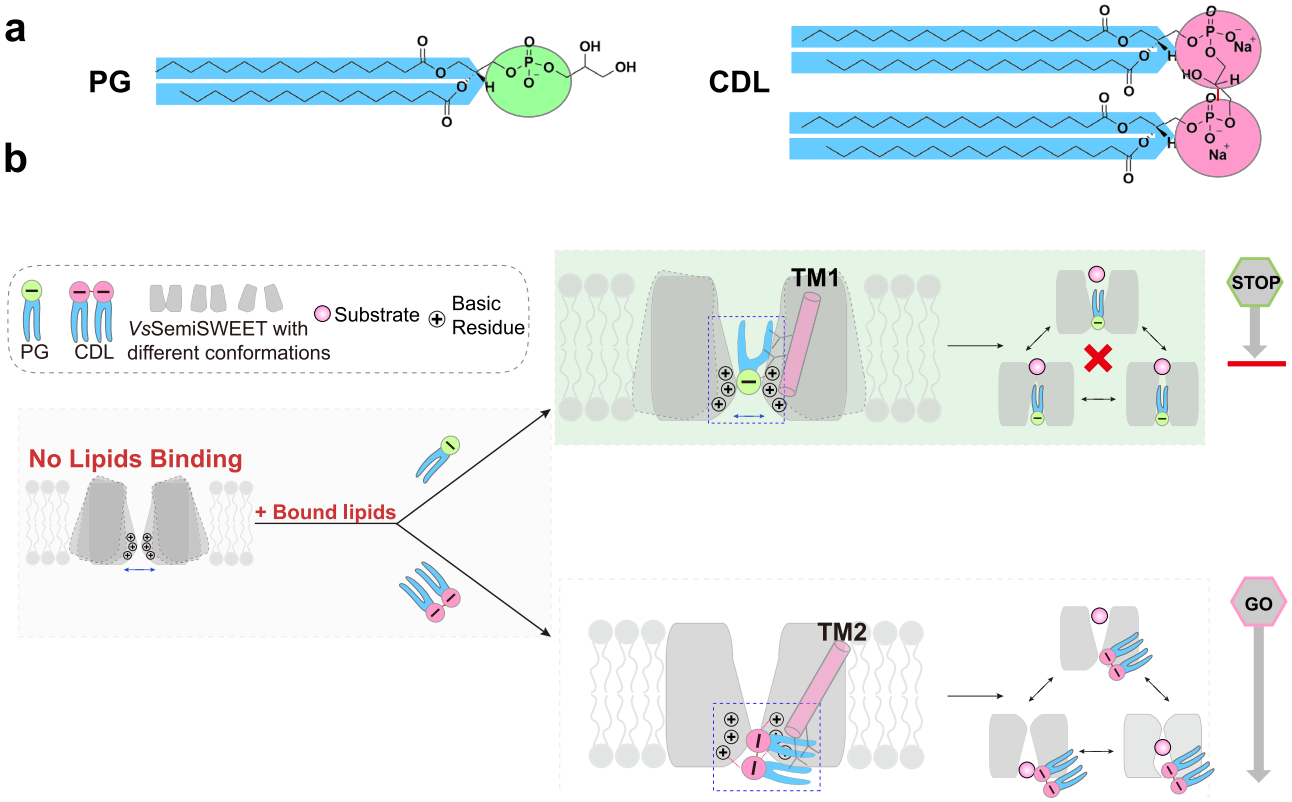

Fig. 7 | Distinct lipid–protein interactions and regulatory mechanisms of CDL and PG in *Vs*SemiSWEET. a Molecular topology comparison: PG (single phosphatidylglycerol headgroup with two acyl chains) versus CDL (dimeric phosphatidylglycerol containing four acyl chains). **b** Regulatory mechanisms: In the absence of lipids, *Vs*SemiSWEET forms unstable dimers due to repulsion between interfacial basic residues. PG acyl tails insert into the interfacial cavity of *Vs*SemiSWEET, disrupting interprotomer interactions and inhibiting the functional transition cycle. In contrast, the acyl tails of CDL interact with TM2, stabilizing the dimeric structure and facilitating functional transitions.

This structural characteristic of CDL impacts distinct properties compared to a combination of two separate PG molecules. For PG, bringing two headgroups into proximity within a binding site incurs both enthalpic and entropic costs. In contrast, the structure of CDL allows for a more favorable arrangement of its phosphate groups without significant energetic penalties, which enhances its interactions with adjacent basic residues. The presence of two phosphate groups in CDL leads to tighter binding with the three basic residues, K32, H37, and H40, due to stronger electrostatic interactions, compared to PG. This observation is consistent with recent MD simulations revealing that CDL molecules exhibit preferential binding to bacterial inner membrane proteins. Notably, these simulations identified over 700 independent CDL binding sites on *E.coli* inner membrane proteins, demonstrating that the proximity of the two phosphate groups in the CDL molecule facilitates interactions with two to three adjacent basic residues[38]. Additionally, the four acyl chains of CDL confer larger hydrophobic volumes compared to PG. This structural feature likely restricts access to the transmembrane cavity while simultaneously stabilizing the conformational integrity of *Vs*SemiSWEET.

The high conservation of basic residues at the binding pockets, particularly the charged residues at positions 32 and 37 on the surface of various SemiSWEET species, highlights the importance of interactions between interfacial lipids and SemiSWEET proteins (Fig. S36). This conservation is likely a result of the co-evolution of lipids and proteins, in which organisms have developed specific lipid profiles to their environmental conditions. Consequently, these lipid profiles shape the evolution of membrane proteins, facilitating diverse lipid–protein interactions that regulate their functions. Such interactions are essential for allowing membrane proteins to adapt to various environments, thereby enhancing their functionality and stability across different physiological contexts.

In summary, our study provides structural and mechanistic insights into a fundamental question of membrane protein biology: how lipid diversity regulates protein behavior through specific interactions. Through a systematic investigation of the interactions between *Vs*SemiSWEET and its specific bound lipids (PE, PG and CDL), our findings reveal that CDL, with its dual phosphates and four acyl chains, modulates the behavior of membrane proteins through interactions involving both the headgroup and the fatty acid. We also demonstrate that the physicochemical properties of the bound lipids play a crucial role in regulating protein conformational stability and functionality. As shown in Fig. 7, the acyl tails of PG insert into the interfacial cavity of *Vs*SemiSWEET, disrupting both the dimer's structure and its functional transition cycle. In contrast, the larger hydrophobic tails of CDL block access to the interfacial pore, thus avoiding disruption of the dimeric architecture. Additionally, the acyl tails of CDL interact with TM2, thereby facilitating a functional conformational transition in *Vs*SemiSWEET. These insights highlight the complexity of specific lipid–protein interactions and emphasize how variations in the acyl tails and headgroups of bound lipids can regulate membrane protein oligomerization and functionality in different ways. Future studies could investigate whether similar lipid-mediated regulatory mechanisms exist in other membrane proteins and explore their roles under physiological or pathological conditions. Such investigations would not only expand our understanding of lipid–protein interactions but also elucidate the molecular

mechanisms underlying membrane protein behavior in diverse biological contexts.

Methods

Sample preparation for solid-state NMR experiments

***Vs*SemiSWEET proteoliposome sample.** Expression and purification. *Vs*SemiSWEET was expressed in *E. coli* BL21(DE3) cells using a pET28a-*Vs*SemiSWEET plasmid with an N-terminal 6×His tag. Colonies of *Vs*SemiSWEET were inoculated into 100 mL of LB media containing kanamycin (100 μg/mL) and grown overnight at 310 K. Then, 20 mL of cell suspension was diluted into 1 L of fresh LB media and allowed to grow at 310 K. When the OD_{600} reached 1.0–1.1, the cells were harvested by centrifugation and resuspended in 250 mL of M9 media (4 g/L ^{13}C glucose, 1 g/L ^{15}N NH_4Cl) and incubated at 310 K for 30 min. Notably, the 2-*Vs*SemiSWEET and 1,3-*Vs*SemiSWEET samples were prepared by substituting glucose in the M9 medium with the corresponding 2-^{13}C– and 1,3-^{13}C–labeled glycerol, respectively. Next, 1 mM IPTG (isopropyl-*β*-D-thiogalactoside) was added to induce protein expression at 310 K. After 5 h, the cells were collected by centrifugation and resuspended in a lysis buffer (20 mM Tris, 100 mM NaCl, pH 8.0), followed by ultrasonication until the solution became clear. The lysate was then subjected to low-speed centrifugation at 4629×*g* for 10 min to remove unbroken cells and larger debris. Total cell membranes were collected by high-speed centrifugation at 58,545×*g* for 1 h. The membranes were dissolved overnight in 1% (w/v) sodium N-lauroylsarcosinate (NLS) at 277 K. *Vs*SemiSWEET was then purified using 2 mL of Ni-IDA resin, with 10 column volumes (CVs) of wash buffer (20 mM Tris, 100 mM NaCl, 20 mM imidazole, 0.2% (w/v) DM, pH 8.0), followed by 5 CVs of elution buffer (20 mM Tris, 100 mM NaCl, 300 mM imidazole, 0.3% DM, pH 8.0). Approximately 30–35 mg of *Vs*SemiSWEET was purified from 1 L of M9 culture.

Reconstitution. The purified *Vs*SemiSWEET was reconstituted into *E. coli* liposomes through a dialysis process. A 5 mg/mL stock of *E. coli* lipids was prepared by hydration and ultrasonication. The lipids were dissolved in 2% (w/v) octyl glucoside (OG) and mixed with the purified *Vs*SemiSWEET at a protein-to-lipid ratio of 1:0.6 (w/w). The mixture was incubated at 291 K for 2 h. Subsequently, the mixture underwent dialysis at 291 K for 6 days against an external solution (20 mM Tris, pH 8.0). The *Vs*SemiSWEET protein–liposomes were collected through ultracentrifugation at 419,832×*g* for 3 h, followed by freeze-drying. The dried complexes were then rehydrated with 30% (w/w) water and packed into a 3.2 mm rotor (thin-wall) for solid-state NMR experiments.

***Vs*SemiSWEET cellular membrane sample.** Expression of *Vs*SemiSWEET. The method used for *Vs*SemiSWEET expression was similar to that described in the preparation of the *Vs*SemiSWEET proteoliposome sample. However, the OD_{600} value of the cells before switching from unlabeled to isotopically enriched media was adjusted from 1.0–1.1 to 1.3–1.4, and the incubation time prior to adding IPTG was reduced from 30 to 10 min.

Cellular membrane isolation. The cell membranes obtained from 250 mL of culture of isotope-labeled cells were resuspended in a lysis buffer (20 mM Tris, 100 mM NaCl, pH 8.0) and sonicated until the solution became clear. To separate the inner and outer membrane fractions, sucrose gradient centrifugation was employed. Specifically, 2.7 mL of 60% (w/v) sucrose, 3.5 mL of 51% (w/v) sucrose, 3 mL of 35% (w/v) sucrose, and 4 mL of the sample were sequentially added to the buffer system (20 mM Tris, 100 mM NaCl, pH 8.0). The gradients were centrifuged in an SW-40 Ti rotor (Beckman) at 169,818×*g* for 16 h. The inner membranes were harvested from the interface between the 35 and 51% sucrose layers using a syringe, while the outer membranes were collected from the interface between the 51 and 60% sucrose layers. For the inner membrane sample, 2 mL was diluted with water to fill an 8.9 mL Beckman centrifuge tube, which was then centrifuged at 419,832×*g* for 3 h to collect the inner membranes. After freeze-drying, the inner membranes were rehydrated with 30% (w/w) water and packed into a 3.2 mm thin-wall rotor for solid-state NMR experiments.

^{13}C-labeled total *E. coli* lipid extract. To assign the chemical shifts of the *E. coli* lipids, we prepared a sample of ^{13}C-labeled extracts from the total *E. coli* lipids[60]. Briefly, *E. coli* BL21(DE3) cells were cultured in M9 medium, using ^{13}C glucose as the sole carbon source. After an overnight culture, the cells were harvested by centrifugation at 6000×*g* for 15 min, yielding a wet mass of 15–20 g from 1 L of M9 culture. The cell pellet (10 mg) was resuspended in 20 mL of chloroform and 40 mL of methanol, followed by filtration. Subsequently, 20 mL of chloroform and 20 mL of distilled water were added. The mixture was transferred to a separator funnel and allowed to stand at 277 K for 24 h. The ^{13}C-labeled *E. coli* total lipids were collected from the lower chloroform phase.

Unfolding and refolding approach for *Vs*SemiSWEET. Unfolding of *Vs*SemiSWEET. The method used for *Vs*SemiSWEET expression was similar to that described in the preparation of the *Vs*SemiSWEET proteoliposome samples. The obtained 250 mL of cells were collected by centrifugation and resuspended in a lysis buffer (20 mM Tris, 100 mM NaCl, pH 8.0), followed by ultrasonication until the solution became clear. The lysate was then subjected to low-speed centrifugation at 4629×*g* for 10 min to remove unbroken cells and larger debris. Total cell membranes were collected by high-speed centrifugation at 58,545×*g* for 1 h. The membranes were dissolved overnight in 1% (w/v) NLS at 277 K. *Vs*SemiSWEET was subsequently purified using 2 mL of Ni-IDA resin, followed by sequential washing steps with 15 mL of buffer A (20 mM Tris, 100 mM NaCl, 0.2% (w/v) NLS, pH 8.0), and 10 mL of buffer B (8 M Urea, 150 mM NaCl, and lysis buffer in a 1:1 volume ratio) to initiate the unfolding of *Vs*SemiSWEET. Further denaturation of the protein was achieved by treating it with 140 mL of Buffer C (8 M Urea and 150 mM NaCl). Finally, to obtain a fully denatured *Vs*SemiSWEET solution, 10 mL of Buffer D (8 M Urea, 150 mM NaCl, 1% formic acid, and 0.2% SDS) was added, and the mixture was left in a 298 K incubator overnight.

Refolding of *Vs*SemiSWEET. An appropriate volume of 2 M Tris solution (pH 8.0) was added to the denatured *Vs*SemiSWEET solution to achieve a final Tris concentration of 50 mM, enhancing its buffering capacity. Next, NaOH solution was gradually added to raise the pH of the protein solution from 2.8 to ~8.0. The lipids were dissolved in 2% (w/v) OG and mixed with the purified *Vs*SemiSWEET at a protein-to-lipid ratio of 1:1 (w/w). The mixture was then incubated overnight at 310 K.

Delipidation of *Vs*SemiSWEET. Detergent washing was employed to remove lipids loosely bound to *Vs*SemiSWEET. In the purification of *Vs*SemiSWEET, the membranes were dissolved overnight in 1% (w/v) NLS at 277 K. *Vs*SemiSWEET was then purified using 2 mL of Ni-IDA resin and subjected to washing with 15 mL of wash buffer (20 mM Tris, 100 mM NaCl, 20 mM imidazole, 0.2% (w/v) DM, pH 8.0). After washing with buffer containing 1% DDM, *Vs*SemiSWEET was eluted in an elution buffer (20 mM Tris, 100 mM NaCl, 300 mM imidazole, 0.3% DM, pH 8.0), and concentrated to ~0.5 mg/mL.

H/D exchange of *Vs*SemiSWEET proteoliposome. The liposome pellets of *Vs*SemiSWEET were suspended in D_2O and incubated with slow shaking at room temperature for 72 h. Subsequently, the pellets were collected through ultracentrifugation at 548,352×*g* for 2 h. The pellets were freeze-dried to remove moisture and then rehydrated with 30% D_2O for subsequent solid-state NMR experiments.

Solid-state NMR experiments

All solid-state NMR experiments were performed at 272 K on an 800 MHz Bruker Avance spectrometer equipped with a 3.2 mm three-channel E-free T3-HXY MAS probe, at a MAS frequency of 10.5 kHz. The typical 90° pulse length for ^{1}H was 3.1 µs, and the 90° pulse lengths for ^{13}C and ^{15}N were 4.5 and 6.6 µs, respectively. The chemical shifts of ^{13}C and ^{15}N were indirectly calibrated using adamantane as an external referencing standard (40.48 ppm for the downfield carbon). During the acquisition and indirect chemical shift evolution process, SPINAL-64 decoupling on the ^{1}H channel was set to 70–75 kHz. In the 2D and 3D solid-state NMR experiments, SPECIFIC CP[61] was employed in polarization transfer between ^{13}C and ^{15}N, and ^{13}C-^{13}C correlations were established through dipolar-assisted rotational resonance (DARR) recoupling[62]. The 2D ^{13}C-^{13}C CORD experiments of 2-*Vs*SemiSWEET and 1,3-*Vs*SemiSWEET samples were used to acquire ^{13}C-^{13}C distance restraints. The 2D ^{1}H-^{13}C INEPT experiment was performed at 298 K, with experimental conditions were optimized for a $^{1}J_{CH}$ coupling constant of 225 Hz. All solid-state NMR experimental data were processed using NMRPipe software[63] and analyzed using Sparky. Detailed parameters for these ssNMR experiments are compiled in Table S5.

Solution NMR experiments

For the ^{31}P NMR study, approximately 0.15 mM of *Vs*SemiSWEET was solubilized in DM in a pH 8.0 buffer (20 mM Tris, 100 mM NaCl, 30 mM imidazole, 0.3% DM, 10% D_2O, pH 8.0). ^{31}P solution-state NMR spectra were collected on a Bruker Avance III spectrometer operating at a magnetic field strength of 11.7 T, corresponding to a proton Larmor frequency of 500 MHz. The spectrometer was equipped with a 5 mm CPP BBO 500S2 BB-H&F-D-05 Z probe and analyzed by TopSpin 4.0.7. The sample temperature was maintained at 315 K.

Extraction of structural restraints

Dihedral angle restraints. Dihedral angles were predicted using TALOS+ based on the N, CO, Cα, and Cβ chemical shifts[64]. The backbone chemical shifts were directly adopted from BMRB entry 51331, as the sample preparation protocol and resulting 2D ^{15}N-^{13}Cα and ^{13}C-^{13}C spectra were identical to those in our prior study[33]. Only angles classified as "good" by TALOS+ were used as dihedral angle restraints, with the program providing error values.

Hydrogen bond restraints. Intrahelical hydrogen bond restraints were applied when both the chemical shift index[65] and TALOS+ indicated helical structures for the corresponding residues. The intrahelical hydrogen bond restraint was defined as the distance between the donor oxygen (O_i) and the acceptor nitrogen (N_{i+4}), and it was set within the range of 1.5 to 3.5 Å.

^{13}C-^{13}C distance restraints. ^{13}C-^{13}C distance restraints were derived from 2D ^{13}C-^{13}C CORD spectra with a mixing time of 500 ms for 2-*Vs*SemiSWEET and 1,3-*Vs*SemiSWEET samples. The signals corresponding to ^{13}C-^{13}C distance restraints were assigned based on the following criteria: (1) The peaks that could be assigned as ^{13}C-^{13}C distance constraints exhibited symmetry, were well-resolved, and had a sufficient signal-to-noise ratio (SNR ≥ 6) in the 2D CORD spectra. (2) All possible assignments of the cross peaks were collected. A tolerance of approximately 0.2 ppm was set for both direct and indirect dimensional ^{13}C chemical shifts, considering the linewidth of the peaks (0.2 to 0.6 ppm) in the CORD spectra. (3) Ambiguity in the assignments was reduced through the following procedures: (i) The ambiguity in the assignment of intra-monomer correlations was notably reduced by utilizing the *Vs*SemiSWEET monomer structure predicted by CS-Rosetta based on the assigned chemical shifts. (ii) If a peak could not be assigned as an intra-monomer correlation, it was classified as a possible inter-monomer correlation. Moreover, the assignments of inter-monomer correlations were confirmed based on the corresponding signal intensities obtained in the 2D ^{13}C-^{13}C spectra recorded on the [(1:2)2-^{13}C/NA] *Vs*SemiSWEET sample.

*Vs*SemiSWEET dimer structure determination in lipid bilayers

Step 1: Monomer *Vs*SemiSWEET structure predicted by CS-Rosetta. The initial monomeric structure of *Vs*SemiSWEET was predicted using the standard POMONA/CS-RosettaCM protocol from the CS-Rosetta package[66,67]. A set of 80 backbone ^{15}N, ^{13}Cα, ^{13}CO, and 72 ^{13}Cβ chemical shifts were utilized as input for the fragment and template selection process. During the subsequent structure generation, only fragments and templates derived from PDB proteins with less than 30% sequence similarity to SemiSWEETs were employed. Additionally, 28 ambiguous long-range intra-monomer distance restraints, determined based on chemical shift specificity, were incorporated for structural prediction. A total of 10,000 all-atom models were generated, from which the ten lowest-energy models were selected as the initial monomeric structures of *Vs*SemiSWEET for further analysis. The RMSD of the backbone heavy atoms for the ten lowest-energy models was 0.9 ± 0.2 Å.

Step 2: Assignments of intra-monomer distance constraints. In the 2D ^{13}C-^{13}C CORD spectra of 2-*Vs*SemiSWEET and 1,3-*Vs*SemiSWEET samples, only isolated peaks with diagonal symmetry, suitable linewidths (0.2 to 0.6 ppm), and sufficient signal-to-noise ratios (SNR ≥6) were assigned. To reduce ambiguity in the assignment of intra-monomer distance constraints, the monomer structures of *Vs*SemiSWEET predicted by CS-Rosetta were utilized. In this step, possible assignments involving intra-monomer distances for correlated atoms exceeding an upper limit of 9.0 Å in the monomer structure were excluded.

Step 3: Monomer *Vs*SemiSWEET structure determination by Xplor-NIH. The *Vs*SemiSWEET monomer structures were calculated by using the Xplor-NIH program (version 2.47)[68]. Standard terms for bond lengths, bond angles, and improper angles were employed to enforce correct covalent geometry. Statistical torsion angle potentials and gyration volume terms were applied, and the hydrogen bond database term HBPot was used to improve hydrogen bond geometry. Folding calculations for full-length single-stranded *Vs*SemiSWEET were derived from first-order sequence extensions of the chain. A total of 522 structures were generated using molecular dynamics simulated annealing in torsion angle space. The calculations involved two consecutive annealing schedules followed by final gradient minimization in Cartesian space. Each *Vs*SemiSWEET structure contained 344 non-redundant ^{13}C-^{13}C distance constraints, 88 hydrogen bond constraints, and 78 torsion angle constraints derived from TALOS-N. The structural calculations began with constant temperature molecular dynamics at 3500 K, running for 800 ps or 10,000 steps, with the time step adjusted to maintain constant energy within tolerance. The temperature was gradually reduced in steps of 25 K. At each temperature, the kinetics were simulated for 2 ps or 500 steps, whichever was shorter. The force constant for the distance constraint was increased from 5 to 50 kcal mol^{-1} Å^{-2}. During high-temperature kinetics at 3500 K, the dihedral angle constraint was disabled, but was enabled during simulated annealing with a force constant of 200 kcal mol^{-1} rad^{-2}. The slew volume force constant was geometrically extended from 0.002 to 1. After simulated annealing, the structure underwent energy minimization using Powell's energy minimization scheme. This methodology resulted in 200 structures, and the first 10 structures with the lowest energy exhibited an RMSD of 1.5 ± 0.4 Å for backbone atoms.

Step 4: Initial dimer structure of *Vs*SemiSWEET generated by Xplor-NIH docking. The initial dimer structure of *Vs*SemiSWEET in lipid bilayers was calculated using the docking module in Xplor-NIH, combined with six ambiguous inter-monomer distance constraints. The assignments of these inter-monomer correlations were confirmed by

analyzing the corresponding signal intensities observed in the 2D ^{13}C-^{13}C spectra recorded on the 2-*Vs*SemiSWEET and [(1:2)2-^{13}C/NA] *Vs*SemiSWEET samples. Furthermore, these correlations could not be assigned as intra-monomer correlations based on the analysis of *Vs*SemiSWEET monomer structure. The PDBEditor tool was employed to create the initial structure for dimer docking, positioning the lowest-energy *Vs*SemiSWEET monomer structure at two fixed points approximately 100 Å apart in a straight line. The ambiguous inter-monomer distance constraints were applied to the inter-monomer interface of the *Vs*SemiSWEET dimer, with force constants ranging from 20 to 100 kcal mol^{-1} Å^{-2}. Noncrystalline restraints were used to ensure that both monomers in the calculation were identical. This potential allowed the internal coordinates of the *Vs*SemiSWEET monomers to remain fixed during the docking process, enabling changes in the orientation of the monomers while preserving their internal structure. During the annealing process, the hydrogen bond database potential term HBDB was used. Standard bond angles and lengths were set using the terms BOND, ANGL, and IMPR. van der Waals forces were applied with force constants ranging from 0.05 to 5.0 kcal mol^{-1} Å^{-2}. Torsion angle kinetics were performed for 5000 steps at 3500 K, followed by annealing to 25 K in increments of 12.5 K for 100 steps at each temperature. After annealing, final energy minimization of the torsion angles and Cartesian coordinates was conducted. The resulting structures were sorted by energy, considering all potential energies determined from the calculations. From the final set of 100 structures, the ten structures with the lowest energy were selected for subsequent analysis.

Step 5: Assignment of the inter-monomer distance constraints. The ten initial *Vs*SemiSWEET dimer structures obtained through docking were used to identify inter-monomer distance constraints. The assignment of intermonomer correlations in the 2D CORD spectra followed the following criteria: (I) Only the peaks that could not be assigned to intra-monomer contacts and that exhibited a noticeable decrease in intensity (>1/3) or even disappearance in the spectra of the [(1:2)2-^{13}C/NA] *Vs*SemiSWEET sample, compared to the corresponding peaks in the spectra of the 2-*Vs*SemiSWEET sample, were assigned as unambiguous intermonomer distance constraints. (II) Only peaks with diagonal symmetry, suitable linewidths (0.2 to 0.6 ppm), and sufficient SNR (≥6) in the CORD spectra were assigned. (III) If a peak satisfies both intra-monomer and inter-monomer distance constraints, and the signal intensity in the spectrum of the [(1:2)2-^{13}C/NA] *Vs*SemiSWEET sample is significantly reduced or even disappears, it was considered an ambiguous inter-monomer constraint; otherwise, it was regarded as an intra-monomer distance constraint.

Step 6: Calculation of the *Vs*SemiSWEET dimer structure by Xplor-NIH. The folding calculations for the full-length single-stranded *Vs*SemiSWEET were extrapolated from first-order sequence extensions of the chain. The two monomers were constrained to maintain identical structures during the annealing process through the non-crystallographic symmetry term PosDiffPot and the translational symmetry term DistSymmPot. A total of 1000 structures were de novo generated through molecular dynamics simulated annealing in torsion angle space with two consecutive annealing schedules, followed by final gradient minimization in Cartesian space. The structure calculation utilized the obtained intra-monomer and intermonomer distance restraints derived from NMR spectra, dihedral angle restraints, and intrahelical hydrogen bonds.

The structural calculations began with constant temperature molecular dynamics at 3500 K, running for 800 ps or 10,000 steps, with the time step allowed to adjust to maintain constant energy within tolerance. The temperature was gradually reduced in steps of 25 K. At each temperature, the kinetics were simulated for 2 ps or 500 steps, whichever was shorter. The force constant for the distance constraint was increased from 1 to 300 kcal mol^{-1} Å^{-2}. During high-temperature kinetics at 3500 K, the dihedral angle constraint was disabled but enabled during simulated annealing with a force constant of 300 kcal mol^{-1} rad^{-2}. The slew volume force constant was geometrically extended from 0.002 to 1. After simulated annealing, the structure underwent energy minimization using Powell's energy minimization scheme. This methodology resulted in 1024 structures, and the first 10 structures with the lowest energy exhibited an RMSD of 0.9 ± 0.3 Å for backbone atoms.

Molecular dynamics simulations

The initial structure of *Vs*SemiSWEET in MD simulations is based on the solid-state NMR structure reconstituted in *E. coli* liposome. The membrane bilayer consists of 1-palmitoyl-2-oleoyl-sn-glycero-3-phosphoethanolamine (POPE) 1-palmitoyl-2-oleoyl-*sn*-glycero-3-phosphoglycerol (POPG), and cardiolipin (CDL). The lipid molar ratio is POPE:POPG:CDL = 75:13:12, which mimics the lipid composition found in *E. coli* membranes[69]. The total number of lipids in the membrane model was 300, composed of 224 POPE, 40 POPG, and 36 CDL molecules, reflecting a physiologically relevant ratio. For the conventional MD (cMD) simulations used to analyze lipid residence times around *Vs*SemiSWEET, three independent replicas of 3 μs each were carried out per system. The reported lipid residence times are averages derived from these replica simulations. For the PG-bound system, four additional POPG lipids were docked to the binding sites of *Vs*SemiSWEET using MOE[70]. In the CDL-bound system, two CDL molecules, each containing two phosphate groups, were docked to the binding sites of *Vs*SemiSWEET. The membrane bilayer model and protein insertion were accomplished using the CHARMM-GUI web server[71]. The CHARMM36 force fields were utilized for both proteins and membranes[72], while the TIP3P model[73] was adopted for water molecules.

The systems underwent energy minimization for 5000 steps using the steepest descent method. During these minimization steps, proteins and lipids were restrained with force constants of 10 kJ/mol × Å^2 and 2.5 kJ/mol × Å^2, respectively. NVT equilibration steps, constrained to the positions of protein-heavy atoms and lipids, were conducted for 500 ps. Subsequently, several 1-ns NPT simulations were performed, during which position constraints on the protein and lipid heavy atoms were gradually reduced to equilibrate the systems. The LINCS algorithm[50] was used to constrain the bond lengths involving hydrogen atoms. A semi-isotropic scheme was employed to independently couple the lateral and perpendicular pressures. Long-range electrostatics were calculated using the Particle-Mesh Ewald method[74] with a cutoff distance of 12 Å. The temperature was maintained at 300 K using the V-rescale method[75], and pressure was controlled by the Parrinello-Rahman barostat[76]. Production runs were executed with a 2-fs time step using the CUDA-accelerated version of the AMBER suite package[77].

Free energy simulations were performed using well-tempered metadynamic simulations[78,79]. Two collective variables (CV), d_{out} and d_{in}, were employed to characterize the opening of the extracellular and intracellular gates on *Vs*SemiSWEET. d_{out} calculated the distances between Cα atom on residue Y62 in each protomer, while d_{in} calculated the distances between the Cα atoms of residues L42–L44 in each protomer. The bias factor γ, which controls the added bias in a history-dependent manner, was set to 32. The height of the initial bias energy was set at 1.0 kJ mol^{-1} and the width was set at 0.5 Å. The bias was added every 2 ps. The GROMACS2022 software[80] with the plumed 2.8 plugin was utilized to perform the metadynamics simulations. The simulation details, including the number of atoms, number of water molecules, box sizes, salt concentration, and lipid compositions, are summarized in Table S6. The convergence tests of simulations are analyzed based on the free energy surface deviation along the simulation time and are given in Fig. S37.

Reporting summary

Further information on research design is available in the Nature Portfolio Reporting Summary linked to this article.

Data availability

Solid-state NMR chemical shifts have been deposited in the Biological Magnetic Resonance Bank (BMRB) with ID number 51331. The atomic coordinates for the solid-state NMR structure have been deposited in the Protein Data Bank (PDB) under accession code 9KON (Structure of *Vs*SemiSWEET in lipid bilayers determined by solid-state NMR). Published structure discussed or analyzed in this work: 4QND. All relevant data that support the findings of this study are provided in the article and supplementary Information. Source data are provided as a Source Data file.

References

1. Gupta, K. et al. The role of interfacial lipids in stabilizing membrane protein oligomers. *Nature* **541**, 421–424 (2017).
2. Laganowsky, A. et al. Membrane proteins bind lipids selectively to modulate their structure and function. *Nature* **510**, 172–174 (2014).
3. Drew, D. & Boudker, O. Ion and lipid orchestration of secondary active transport. *Nature* **626**, 963–974 (2024).
4. Cong, X., Liu, Y., Liu, W., Liang, X. W. & Laganowsky, A. Allosteric modulation of protein-protein interactions by individual lipid binding events. *Nat. Commun.* **8**, 2203 (2017).
5. Koshy, C. et al. Structural evidence for functional lipid interactions in the betaine transporter BetP. *EMBO J.* **32**, 3096–3105 (2013).
6. Debruycker, V. et al. An embedded lipid in the multidrug transporter LmrP suggests a mechanism for polyspecificity. *Nat. Struct. Mol. Biol.* **27**, 829–835 (2020).
7. Schmidpeter, P. A. M. et al. Anionic lipids unlock the gates of select ion channels in the pacemaker family. *Nat. Struct. Mol. Biol.* **29**, 1092–1100 (2022).
8. Landreh, M. et al. Integrating mass spectrometry with MD simulations reveals the role of lipids in Na^+/H^+ antiporters. *Nat. Commun.* **8**, 13993 (2017).
9. Schrecke, S. et al. Selective regulation of human TRAAK channels by biologically active phospholipids. *Nat. Chem. Biol.* **17**, 89–95 (2021).
10. Pyle, E. et al. Structural lipids enable the formation of functional oligomers of the eukaryotic purine symporter UapA. *Cell Chem. Biol.* **25**, 840–848 (2018).
11. Lee, A. G. Lipid-protein interactions. *Biochem. Soc. Trans.* **39**, 761–766 (2011).
12. Ernst, M. & Robertson, J. L. The role of the membrane in transporter folding and activity. *J. Mol. Biol.* **433**, 167103 (2021).
13. Borcik, C. G. et al. The lipid activation mechanism of a transmembrane potassium channel. *J. Am. Chem. Soc.* **142**, 14102–14116 (2020).
14. Schmidpeter, P. A. M. et al. Membrane phospholipids control gating of the mechanosensitive potassium leak channel TREK1. *Nat. Commun.* **14**, 1077 (2023).
15. Kumar, P., Cymes, G. D. & Grosman, C. Structure and function at the lipid-protein interface of a pentameric ligand-gated ion channel. *Proc. Natl. Acad. Sci. USA* **118**, e2100164118 (2021).
16. Petroff, J. T. et al. Open-channel structure of a pentameric ligand-gated ion channel reveals a mechanism of leaflet-specific phospholipid modulation. *Nat. Commun.* **13**, 7017 (2022).
17. Wang, S. H. et al. Structures of the Mycobacterium tuberculosis efflux pump EfpA reveal the mechanisms of transport and inhibition. *Nat. Commun.* **15**, 7710 (2024).
18. Agasid, M. T. & Robinson, C. V. Probing membrane protein-lipid interactions. *Curr. Opin. Struct. Biol.* **69**, 78–85 (2021).
19. Bolla, J. R., Agasid, M. T., Mehmood, S. & Robinson, C. V. Membrane protein-lipid interactions probed using mass spectrometry. *Annu. Rev. Biochem.* **88**, 85–111 (2019).
20. Drew, D., North, R. A., Nagarathinam, K. & Tanabe, M. Structures and general transport mechanisms by the major facilitator superfamily (MFS). *Chem. Rev.* **121**, 5289–5335 (2021).
21. Jia, B. L. et al. Integrative view of the diversity and evolution of SWEET and SemiSWEET sugar transporters. *Front. Plant Sci.* **8**, 319166 (2017).
22. Feng, L. & Frommer, W. B. Structure and function of SemiSWEET and SWEET sugar transporters. *Trends Biochem. Sci.* **40**, 480–486 (2015).
23. Latorraca, N. R. et al. Mechanism of substrate translocation in an alternating access transporter. *Cell* **169**, 96–107 (2017).
24. Lee, Y., Nishizawa, T., Yamashita, K., Ishitani, R. & Nureki, O. Structural basis for the facilitative diffusion mechanism by SemiSWEET transporter. *Nat. Commun.* **6**, 6112 (2015).
25. Xu, Y. et al. Structures of bacterial homologues of SWEET transporters in two distinct conformations. *Nature* **515**, 448–452 (2014).
26. Wang, J. et al. Crystal structure of a bacterial homologue of SWEET transporters. *Cell Res.* **24**, 1486–1489 (2014).
27. Gupta, K. et al. Identifying key membrane protein lipid interactions using mass spectrometry. *Nat. Protoc.* **13**, 1106–1120 (2018).
28. Deng, Z. X., Yuan, B. & Yang, K. Cardiolipin selectively binds to the interface of VsSemiSWEET and regulates its dimerization. *J. Phys. Chem. Lett.* **12**, 1940–1946 (2021).
29. Weingarth, M. et al. Structural determinants of specific lipid binding to potassium channels. *J. Am. Chem. Soc.* **135**, 3983–3988 (2013).
30. Yekefallah, M. et al. Cooperative gating of a K^+ channel by unmodified biological anionic lipids viewed by solid-state NMR spectroscopy. *J. Am. Chem. Soc.* **146**, 4421–4432 (2024).
31. Huster, D. Solid-state NMR spectroscopy to study protein lipid interactions. *Biochim. Biophys. Acta Mol. Cell Biol. Lipids* **1841**, 1146–1160 (2014).
32. van der Cruijsen, E. A. W. et al. Importance of lipid-pore loop interface for potassium channel structure and function. *Proc. Natl. Acad. Sci. USA* **110**, 13008–13013 (2013).
33. Zhang, Y. et al. Solid-state NMR ^{13}C and ^{15}N resonance assignments of *Vibrio* sp. SemiSWEET transporter in lipid bilayers. *Biomol. NMR Assign.* **16**, 325–332 (2022).
34. Hou, G. J., Yan, S., Trébosc, J., Amoureux, J. P. & Polenova, T. Broadband homonuclear correlation spectroscopy driven by combined $R2_n^v$ sequences under fast magic angle spinning for NMR structural analysis of organic and biological solids. *J. Magn. Reson.* **232**, 18–30 (2013).
35. Laage, S., Tao, Y. S. & McDermott, A. E. Cardiolipin interaction with subunit c of ATP synthase: Solid-state NMR characterization. *Biochim. Biophys. Acta Biomembr.* **1848**, 260–265 (2015).
36. van Beekveld, R. A. M. et al. Specific lipid studies in complex membranes by solid-state NMR spectroscopy. *Chem. Eur. J.* **28**, e202202472 (2022).
37. Hariharan, P. et al. Structural and functional characterization of protein-lipid interactions of the Salmonella typhimurium melibiose transporter MelB. *BMC Biol.* **16**, 85 (2018).
38. Corey, R. A. et al. Identification and assessment of cardiolipin interactions with *E. coli* inner membrane proteins. *Sci. Adv.* **7**, eabh2217 (2021).
39. Ames, G. F. Lipids of *Salmonella typhimurium* and *Escherichia coli*: structure and metabolism. *J. Bacteriol.* **95**, 833–843 (1968).
40. Danevcic, T., Rilfors, L., Strancar, J., Lindblom, G. & Stopar, D. Effects of lipid composition on the membrane activity and lipid phase behaviour of *Vibrio* sp DSM14379 cells grown at various NaCl concentrations. *Biochim. Biophys. Acta Biomembr.* **1712**, 1–8 (2005).

41. Engberg, O. et al. Rhomboid-catalyzed intramembrane proteolysis requires hydrophobic matching with the surrounding lipid bilayer. *Sci. Adv.* **8**, eabq8303 (2022).
42. Warschawski, D. E., Arnold, A. A. & Marcotte, I. A new method of assessing lipid mixtures by ^{31}P magic-angle spinning NMR. *Biophys. J.* **114**, 1368–1376 (2018).
43. de Vlugt, J. E. et al. Identifying lipids tightly bound to an integral membrane protein. *Biochim. Biophys. Acta Biomembr.* **1862**, 183345 (2020).
44. Castellani, F. et al. Structure of a protein determined by solid-state magic-angle-spinning NMR spectroscopy. *Nature* **420**, 98–102 (2002).
45. Xie, H. Y. et al. Solid-state NMR structure determination of a membrane protein in *E. coli* cellular inner membrane. *Sci. Adv.* **9**, eadh4168 (2023).
46. Wang, S. L. et al. Solid-state NMR spectroscopy structure determination of a lipid-embedded heptahelical membrane protein. *Nat. Methods* **10**, 1007–1012 (2013).
47. Bayro, M. J. et al. Dipolar truncation in magic-angle spinning NMR recoupling experiments. *J. Chem. Phys.* **130**, 114506 (2009).
48. Roy, R. & Al-Hashimi, H. M. AlphaFold3 takes a step toward decoding molecular behavior and biological computation. *Nat. Struct. Mol. Biol.* **31**, 997–1000 (2024).
49. Good, D. B. et al. Conformational dynamics of a seven transmembrane helical protein *Anabaena* sensory rhodopsin probed by solid-state NMR. *J. Am. Chem. Soc.* **136**, 2833–2842 (2014).
50. Hess, B., Bekker, H., Berendsen, H. J. C. & Fraaije, J. LINCS: a linear constraint solver for molecular simulations. *J. Comput. Chem.* **18**, 1463–1472 (1997).
51. Kumar, S. et al. Native mass spectrometry of membrane protein-lipid interactions in different detergent environments. *Anal. Chem.* **96**, 16768–16776 (2024).
52. Flegler, V. J. et al. Mechanosensitive channel gating by delipidation. *Proc. Natl. Acad. Sci. USA* **118**, e2107095118 (2021).
53. Cowan, A. D. et al. BAK core dimers bind lipids and can be bridged by them. *Nat. Struct. Mol. Biol.* **27**, 1024–1031 (2020).
54. Chen, L. Q., Cheung, L. S., Feng, L., Tanner, W. & Frommer, W. B. Transport of sugars. *Annu. Rev. Biochem.* **84**, 865–894 (2015).
55. Musatov, A. & Sedlák, E. Role of cardiolipin in stability of integral membrane proteins. *Biochimie* **142**, 102–111 (2017).
56. Zigoneanu, I. G., Yang, Y. J., Krois, A. S., Haque, M. E. & Pielak, G. J. Interaction of α-synuclein with vesicles that mimic mitochondrial membranes. *Biochim. Biophys. Acta Biomembr.* **1818**, 512–519 (2012).
57. Govaerts, C. Lipids can make them stick together. *Trends Biochem. Sci.* **42**, 329–330 (2017).
58. Rimon, A., Mondal, R., Friedler, A. & Padan, E. Cardiolipin is an optimal phospholipid for the assembly, stability, and proper functionality of the dimeric form of NhaA Na^+/H^+ antiporter. *Sci. Rep.* **9**, 17662 (2019).
59. Reading, E. et al. Interrogating membrane protein conformational dynamics within native lipid compositions. *Angew. Chem. Int. Ed.* **56**, 15654–15657 (2017).
60. Nickels, J. D. et al. *Bacillus subtilis* lipid extract, a branched-chain fatty acid membrane model. *J. Phys. Chem. Lett.* **8**, 4214–4217 (2017).
61. Baldus, M., Petkova, A. T., Herzfeld, J. & Griffin, R. G. Cross polarization in the tilted frame: assignment and spectral simplification in heteronuclear spin systems. *Mol. Phys.* **95**, 1197–1207 (1998).
62. Takegoshi, K., Nakamura, S. & Terao, T. ^{13}C-^{1}H dipolar-assisted rotational resonance in magic-angle spinning NMR. *Chem. Phys. Lett.* **344**, 631–637 (2001).
63. Delaglio, F. et al. NMRPipe: a multidimensional spectral processing system based on UNIX pipes. *J. Biomol. NMR* **6**, 277–293 (1995).
64. Luca, S. et al. Secondary chemical shifts in immobilized peptides and proteins: a qualitative basis for structure refinement under magic angle spinning. *J. Biomol. NMR* **20**, 325–331 (2001).
65. Wishart, D. S., Sykes, B. D. & Richards, F. M. The chemical shift index: a fast and simple method for the assignment of protein secondary structure through NMR spectroscopy. *Biochemistry* **31**, 1647–1651 (1992).
66. Shen, Y. et al. Consistent blind protein structure generation from NMR chemical shift data. *Proc. Natl. Acad. Sci. USA* **105**, 4685–4690 (2008).
67. Shen, Y. & Bax, A. Homology modeling of larger proteins guided by chemical shifts. *Nat. Methods* **12**, 747–750 (2015).
68. Bermejo, G. A., Tjandra, N., Clore, G. M. & Schwieters, C. D. Xplor-NIH: better parameters and protocols for NMR protein structure determination. *Protein Sci.* **33**, e4922 (2024).
69. Shokri, A. & Larsson, G. Characterisation of the *Escherichia coli* membrane structure and function during fedbatch cultivation. *Microb. Cell Fact.* **3**, 9 (2004).
70. Vilar, S., Cozza, G. & Moro, S. Medicinal chemistry and the molecular operating environment (MOE): application of QSAR and molecular docking to drug discovery. *Curr. Top. Med. Chem.* **8**, 1555–1572 (2008).
71. Jo, S., Kim, T., Iyer, V. G. & Im, W. Software news and updates - CHARNIM-GUI: a web-based graphical user interface for CHARMM. *J. Comput. Chem.* **29**, 1859–1865 (2008).
72. Vanommeslaeghe, K. et al. CHARMM general force field: a force field for drug-like molecules compatible with the CHARMM all-atom additive biological force fields. *J. Comput. Chem.* **31**, 671–690 (2010).
73. Price, D. J. & Brooks, C. L. A modified TIP3P water potential for simulation with Ewald summation. *J. Chem. Phys.* **121**, 10096–10103 (2004).
74. Darden, T., York, D. & Pedersen, L. Particle mesh Ewald: an N·log(N) method for Ewald sums in large systems. *J. Chem. Phys.* **98**, 10089–10092 (1993).
75. Bussi, G., Donadio, D. & Parrinello, M. Canonical sampling through velocity rescaling. *J. Chem. Phys.* **126**, 014101 (2007).
76. Ke, Q., Gong, X. T., Liao, S. W., Duan, C. X. & Li, L. B. Effects of thermostats/barostats on physical properties of liquids by molecular dynamics simulations. *J. Mol. Liq.* **365**, 120116 (2022).
77. Case, D. A. et al. The Amber biomolecular simulation programs. *J. Comput. Chem.* **26**, 1668–1688 (2005).
78. Barducci, A., Bussi, G. & Parrinello, M. Well-tempered metadynamics: a smoothly converging and tunable free-energy method. *Phys. Rev. Lett.* **100**, 020603 (2008).
79. Bussi, G. & Laio, A. Using metadynamics to explore complex free-energy landscapes. *Nat. Rev. Phys.* **2**, 200–212 (2020).
80. Páll, S. et al. Heterogeneous parallelization and acceleration of molecular dynamics simulations in GROMACS. *J. Chem. Phys.* **153**, 134110 (2020).

Acknowledgements

This work was funded by grants from the National Natural Science Foundation of China (22434003, 22507127, 22577099, 21927801, 21991081, 21921004, and 22004124), the Chinese Academy of Sciences (YJKYYQ20190032 and XDB0540000), the Hubei Provincial Natural Science Foundation of China (2024AFA005 and 2025AFB512), Start-up Research Funding for Newly Recruited Faculty at Nanjing Medical University (KY101RC20250008), and the China Postdoctoral Science Foundation (2020M672455, 2024M752494, and GZC20241290).

Author contributions

Y.Z. and J.Y. conceived the study. Y.Z., M.D., and J.Y. designed the experiments. J.L., W.Z., and Q.T. performed biochemistry experiments.

W.Z. Y.-X.Z. and Y.Z. prepared the NMR samples. Y.Z. performed NMR experiments. Y.Z. and H.X. performed structural biology experiments. M.D. constructed the MD simulations. Y.S. built and refined structural models. All authors analyzed the results. Y.Z., W.Z., M.D. and J.Y. interpreted the data and wrote the manuscript.

Competing interests
The authors declare no competing interests.

Additional information
Supplementary information The online version contains supplementary material available at https://doi.org/10.1038/s41467-026-69804-3.

Correspondence and requests for materials should be addressed to Mojie Duan or Jun Yang.

Peer review information *Nature Communications* thanks Antoine Loquet, Carol Robinson, who co-reviewed with Haigang Song, and the other, anonymous, reviewer(s) for their contribution to the peer review of this work. A peer review file is available.